

THESIS FOR THE DEGREE OF DOCTOR OF PHILOSOPHY

Control of Permanent-Magnet Synchronous Machines in Automotive Applications

OSKAR WALLMARK



Division of Electric Power Engineering
Department of Energy and Environment
CHALMERS UNIVERSITY OF TECHNOLOGY
Göteborg, Sweden 2006

Control of Permanent-Magnet Synchronous Machines in Automotive Applications
OSKAR WALLMARK
ISBN 91-7291-846-2

© OSKAR WALLMARK, 2006.

Doktorsavhandlingar vid Chalmers tekniska högskola
Ny serie nr. 2528
ISSN 0346-718X

Division of Electric Power Engineering
Department of Energy and Environment
Chalmers University of Technology
SE-412 96 Göteborg
Sweden
Telephone +46 (0)31-772 1000

Cover: “Salient limit cycle.” Artist: AnnSofie Hahne. Compare also with [Paper I, Fig. 6]
and [Paper III, Fig. 11].

Chalmers Bibliotek, Reproservice
Göteborg, Sweden 2006

To my family

Abstract

This thesis deals with the design and analysis of control system structures for electric drives equipped with permanent-magnet synchronous machines (PMSMs) in automotive applications.

Sensorless control, meaning vector control without a mechanical rotor position sensor, is considered and a speed and position estimator of phase-locked loop type is analyzed thoroughly. Modifications are proposed to allow for operation in the whole speed range and to improve the estimator's capacity to handle large speed estimation errors. It is shown that rotor saliency affects the estimator dynamics which may become unstable for certain parameter selections and operating conditions. Simple parameter selection rules are therefore derived in order to guarantee stability and to simplify an implementation.

Of particular interest for PMSMs with small or negligible rotor saliency, an estimator, extracting position information solely from the back-electromotive force is also considered. The estimator is based on the well known "voltage model" and modifications are proposed in order to improve the estimator's performance in the low-speed range by guaranteeing synchronization at startup and allowing stable rotation reversals.

The theory of loss minimization by means of control is applied to a PMSM drive intended for propulsion in a hybrid electric vehicle. Through stronger field weakening, the fundamental core losses can be reduced at the expense of increased resistive losses. The study shows, however, that the additional inverter losses, due to the addition of extra field weakening, reduce the potential to minimize the total losses considerably.

A review of fault-tolerant PMSM drives is presented and control algorithms are proposed for achieving sensorless control, closed-loop field-weakening control, and maximum utilization of the available inverter voltage for a drive that, for redundancy, adopts an additional inverter leg connected to the neutral point of the machine.

The impact of various electrical faults in a vehicle equipped with in-wheel motors and individual steering actuators is also investigated. Here, it is shown that vehicle stability can be maintained with only minor displacements using a closed-loop path controller and an optimal approach, recently reported in the literature, to allocate tire forces.

Index Terms: Electric drive, electric vehicle, fault tolerance, hybrid electric vehicle, inverter, in-wheel motor, loss minimization, permanent-magnet synchronous machine, phase-locked loop, position estimation, sensorless control, vector control.

Acknowledgements

This research project was fully funded by the Swedish National Energy Agency, within the “Energisystem i vägfordon” research program, which is gratefully acknowledged.

First of all, I would like to thank my supervisor Dr. Ola Carlson for giving me the opportunity to begin my Ph.D. studies and for help and assistance throughout the whole course of this project. I would also like to thank my assistant supervisor Prof. Lennart Harnefors for excellent technical guidance and encouragement. Furthermore, my examiner Prof. Tore Undeland is acknowledged for his valuable comments and strong support.

I am very grateful to my fellow Ph.D. students who have assisted me in several ways. Particularly, Massimo Bongiorno, Stefan Lundberg, Dr. Rolf Ottersten, and Dr. Andreas Petersson have contributed with several interesting discussions and valuable assistance in the lab. Many thanks also go to my other colleagues at the Division of Electric Power Engineering and the former Department of Electric Power Engineering who have supported me during my studies. Particularly Prof. Torbjörn Thiringer and Mr. Robert Karlsson who have assisted with valuable discussions and help with practical matters.

I further would like to thank my co-authors, especially industrial Ph.D. student Mats Jonasson at Volvo Car Corporation for an interesting collaboration that, among other things, provided me with several important insights into the automotive world.

Prof. Robert D. Lorenz at Wisconsin Electric Machines and Power Electronics Consortium (WEMPEC) is acknowledged for allowing me to visit during parts of autumn 2005. I particularly would like to thank Dr. Kan Akatsu, Ph.D. student Michael C. Harke, and Dr. Luiz A. S. Ribeiro for interesting discussions concerning my research as well as making my time at WEMPEC very pleasant.

I am very grateful to Prof. Chandur Sadarangani and Lic. Eng. Mats Leksell at the Royal Institute of Technology. Thank you for allowing me to finalize my thesis as a visitor in the Electric Machines and Power Electronics group during the greater part of 2006.

The members of this project’s reference group, Lic. Eng. Johan Hellsing at Volvo Car Corporation, Mr. Lars Hoffman at Saab Automobile, Lic. Eng. Joachim Lindström at Volvo Technology Corporation, Dr. Rolf Ottersten at GM Powertrain, Mr. Ingemar Söderlund at Saab Automobile, and Dr. Marguerite Touma Holmberg at ABB Automation Products have contributed with fruitful discussions and invaluable industrial input which is gratefully acknowledged.

I would further like to thank all members of my family for believing in me. I love you all very much.

Last, but certainly not least, I would like to thank my fiancée AnnSofie Hahne and our newborn son Arvid for their, in different ways, endless love and support.

Oskar Wallmark
Västerås, Sweden
September 2006

Contents

Abstract	v
Acknowledgements	vii
Contents	ix
1 Introduction	1
1.1 Electric Power in Automotive Applications	1
1.1.1 Drivetrain Configurations	2
1.1.2 Electrical Features in Future Vehicles	3
1.1.3 Permanent-Magnet Machines	3
1.2 Objectives and Scope of Thesis	4
1.3 Outline of Thesis	5
1.4 Scientific Contributions	5
1.5 List of Publications	6
1.5.1 Contributions of Individual Authors	7
2 Modeling of Permanent-Magnet Synchronous Machines	9
2.1 A PMSM Model Including Spatial Harmonics	9
2.1.1 Current Dynamics	12
2.1.2 Electromagnetic Torque	14
2.2 Core Losses	15
2.3 Field-Weakening Operation	16
2.4 Current and Speed Control	17
2.4.1 Current Control	17
2.4.2 Speed Control	18
2.4.3 Experimental Evaluation	19
2.5 Summary of Chapter	20
3 Speed and Position Estimation	21
3.1 Introduction	21
3.1.1 Automotive Applications	22

Contents

3.1.2	Outline of Chapter	22
3.2	Some Properties of a PLL-Type Estimator	22
3.2.1	Experimental Evaluation	24
3.2.2	Linearized Error Dynamics	25
3.2.3	Global Stability	30
3.2.4	Impact of Rotor Saliency	30
3.3	Recent Developments	32
3.3.1	Signal-Injection Based Estimation	32
3.3.2	Back-EMF Based Estimation at Low Speeds	33
3.3.3	Outlook	35
3.4	Summary of Chapter	36
4	On Fault Tolerance and Fault Characteristics of PMSM Drives	37
4.1	Introduction	37
4.2	Fault-Tolerant Machines	38
4.3	Inverter Reliability	39
4.3.1	Response of PMSMs to Inverter Faults	39
4.3.2	Fault-Tolerant Inverters	41
4.3.3	Control Algorithms for a Fault-Tolerant Inverter	43
4.4	Sensor Faults	45
4.5	Electrical Faults in a Propulsion Application	46
4.5.1	A Vehicle With Individual Control of All Four Wheels	47
4.5.2	Simulation Study	48
4.6	Summary of Chapter	51
5	Concluding Remarks	53
5.1	Summary	53
5.2	Proposals for Future Work	54
	References	57
A	Glossary of Symbols, Subscripts, Superscripts, and Abbreviations	65
B	Adopted Per-Unit System and PMSM Parameters	69
B.1	Per-Unit System	69
B.2	PMSM Parameters	69
B.2.1	PMSM1	69
B.2.2	PMSM2	70
C	Selected Publications	71

Chapter 1

Introduction

Aspects of electric power in automotive applications are briefly reviewed in this chapter. The focus is put on electric drives, consisting of electric machines and their corresponding power electronics. The objectives of the work resulting in the present thesis as well the fundamental scientific contributions are presented. Finally, the publications originating from this Ph.D. project are listed.

1.1 Electric Power in Automotive Applications

The first *electric vehicle* (EV) was built around 1834 and the EV concept has thus been around for almost 200 years. However, the EV had almost vanished from the market by 1930. This was mainly because of insufficient range, due to limited battery capacity, as compared to vehicles equipped with *internal combustion engines* (ICEs); a technology that was evolving rapidly at that time [65], [72]. A more mature generation of EVs was born in 1996 when General Motors Corporation leased their EV, named EV-1, to customers in selected states of the U.S.A. Unfortunately, once again, the attempt to introduce EVs to the customer market failed and, essentially, the worst deficiency of EVs is still their limited range [45].

As the demand for more environmental-friendly cars has continued to grow, originating from both individual customers and organizations as well as support by governmental means, i.e., tax incentives and other regulations, the failure of EVs has set the stage for the *hybrid electric vehicle* (HEV). In HEVs, the *internal combustion engine* (ICE) is combined with electric propulsion which offers several possible advantages, at the cost of increased complexity. The main advantages are an increase in range (as compared to EVs), the potential to operate the ICE at optimal (maximization of fuel economy, minimized emissions or a compromise between both) operating points, and the use of regenerative braking. During regenerative braking, the energy used to slow or halt the vehicle is converted into electricity which can charge the built-in battery rather than being wasted as heat. By the combined effect of operation of the ICE at optimal operating points

and regenerative braking, the fuel consumption of an HEV can be significantly reduced as compared to conventional vehicles. The first HEV from a major car manufacturer was the Toyota Prius, released by the Toyota Motor Corporation to the Japanese market in 1997 [45].

1.1.1 Drivetrain Configurations

Today, HEVs are commercially available from several car manufacturers. Depending on how the drivetrain is constituted, HEVs can be classified into different subgroups. Figs. 1.1a) and 1.1b) illustrate the *series-* and *parallel-HEV* configurations.

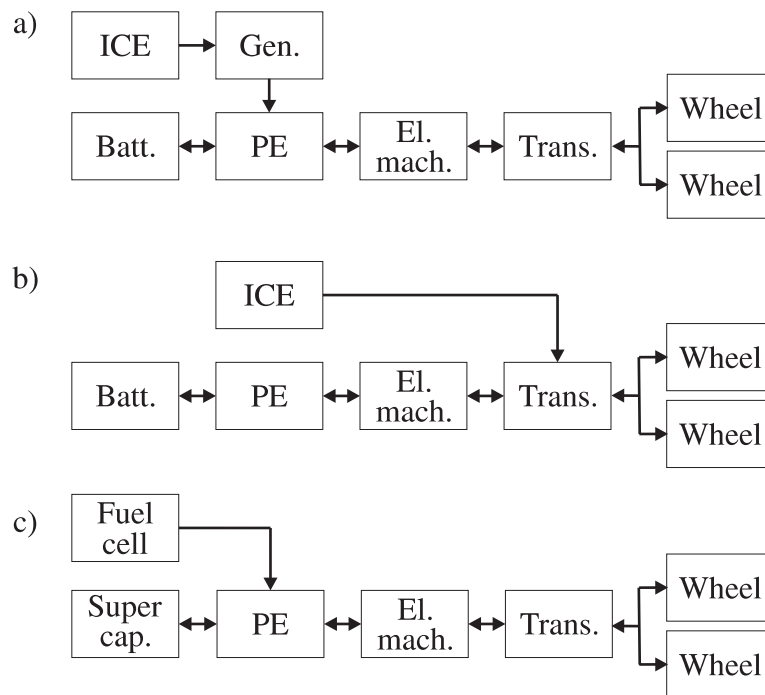


Fig. 1.1 Examples of different vehicle drivetrains (see Appendix A for a glossary of the used abbreviations). The arrows indicate possible directions of energy flow: a) Series-HEV configuration; b) Parallel-HEV configuration; c) Supercapacitor-assisted FCV configuration.

In a series-HEV, there is no mechanical connection between the ICE and the transmission. The power delivered by the ICE is converted into electrical power by the generator. This power can then be used for propulsion or for charging the battery. Advantages of this type of configuration include the potential to choose the operating point of the ICE freely (even turning it off in zero-emission zones) and the flexibility of locating the ICE and generator set. The main disadvantages are the increased number of energy conversions (as compared to the parallel-HEV described below) and that the electric machine and the power electronics need to be sized for the maximum sustained power of the vehicle.

The propulsion power in a parallel-HEV can be supplied by the ICE alone, by the electric machine alone, or by a combination of both. In comparison to the series-HEV, the electric machine and the ICE can be of a smaller size (provided that the battery is never depleted). Even for long-range operation, only the ICE needs to be rated for peak power while the rating of the electric machine can be significantly lower. Another advantage is the absence of the generator which simplifies the configuration.

A wide range of other drivetrains are also currently being developed. As an example, Fig. 1.1c) illustrates the drivetrain of a *fuel-cell vehicle* (FCV) where the propulsion power is generated from a fuel cell assisted by a supercapacitor. For a current discussion on different types of EV and HEV drivetrains, see, e.g. [17] and [23].

1.1.2 Electrical Features in Future Vehicles

Today, there is a strong trend in the automotive industry to replace mechanical and hydraulic loads in vehicles with their electric counterparts. This is due to advantages which include an increase in efficiency as well as comfort and safety related benefits. Table 1.1 (adapted from [23]) lists a selection of electrically assisted functions that are *all* likely to appear in future vehicles. All of the listed functions have already appeared in concept vehicles and some of them are available in commercial vehicles. Several of the functions listed in the table require electric machines and corresponding power electronics with a functionality similar to what used for propulsion, though at much lower power levels.

Table 1.1: Typical electrically assisted functions in future vehicles.

Active suspension	Drive-by-wire
Electric power steering	Electric valve control
Fans and pumps	Ride-height adjustment
Steer-by-wire	Throttle actuation

Table 1.1 is far from complete but it is apparent that the power demand from electrically assisted functions will increase in future vehicles. In [23], it is predicted that the power demand from the electrically assisted functions (excluding propulsion) in future advanced vehicles will reach a value as high as 10 kW.

1.1.3 Permanent-Magnet Machines

Permanent-magnet machines are, due to their high efficiency, power density, and torque-to-inertia ratio a common choice in EV and HEV concepts although other machine types, such as induction and switched-reluctance machines, also have been adopted [14], [17].

Permanent-magnet machines are, depending on the supply voltage waveform, divided into *brushless dc* machines (BLDCs) which are fed with trapezoidal voltage waveforms and *permanent-magnet synchronous machines* (PMSMs) which are fed with sinu-

soidal waveforms [35]. Both types are found in EVs and HEVs. However, in the present thesis the scope is limited and only PMSMs are considered.

As already pointed out, several of the functions listed in Table 1.1 require electric machines and power electronics similar to those used in propulsion applications, although at lower power levels. Additional requirements for these electrically assisted functions could include, e.g., a high mechanical bandwidth or a certain required level of fault tolerance. Also in several of these applications can PMSMs be an attractive choice as well.

1.2 Objectives and Scope of Thesis

As pointed out in Section 1.1.3, adopting PMSM drives in EVs and HEVs can contribute significantly to improve the overall efficiency of the vehicle. Thereby, the operating range can be increased and (for HEVs) the fuel consumption is reduced. In this thesis, control algorithms for PMSM drives that can be applied to a wide range of automotive applications are proposed and analyzed. The main objective is to provide methods and knowledge that simplify the introduction of PMSM drives in EVs and HEVs.

Control of a PMSM without using a rotor-position sensor has obvious advantages in terms of cost, size, and reliability. Thus, several of the contributions presented in this thesis are related to how rotor speed and position can be accurately estimated and how such an estimator could be implemented. This research topic is hardly new and a plethora of different methods have already been presented in the literature. Therefore, the contributions in this thesis that relate to this topic involve a detailed analysis of methods already presented in the literature rather than trying to present entirely novel methods. The results of the analysis provide valuable insights into the properties of the estimators at different operating conditions. Modifications and design guidelines are then proposed in order to simplify an implementation. It is the author's desire that this thesis, along with the Licentiate thesis [74], also should function as a sort of "cookbook" that can be used when implementing a vector-controlled PMSM (with or without the use of a rotor-position sensor) in an automotive application.

With the introduction of modern *digital-signal processors* (DSPs), it is possible to implement advanced control algorithms that can affect the losses of a drive only by control action. This is obviously attractive for drives in EV and HEV applications and is therefore investigated in the form of a case study.

The response of PMSM drives to various electrical faults is also considered in this thesis. The proper operation of certain functions listed in Table 1.1 is critical and failure cannot be tolerated since it would affect passenger safety dramatically. Therefore, means for providing fault tolerance that can be attractive for the functions listed in Table 1.1 are investigated. The impact of electrical faults striking PMSM drives used for propulsion is strongly dependent on how the specific electric drivetrain is constituted. The study of this topic is therefore restricted to two case studies that consider a vehicle equipped with four

in-wheel motors that can be individually controlled.

1.3 Outline of Thesis

This thesis is in the form of a so called “compilation thesis.” The main chapters in the thesis are therefore kept brief and serve to introduce key concepts and provide a background for the scientific contributions which are further presented in the included papers. The chapters are outlined bellow.

Chapter 2 discusses different aspects of modeling PMSMs for control purposes. A PMSM model including the effect of spatial harmonics is derived and the speed and current controllers used in the various experiments are briefly reviewed.

Chapter 3 reviews some general problems related to speed and position estimation when applied to PMSM drives. The estimator presented in [32] is analyzed and improvements, presented further in the included papers, are outlined. Finally, a review of approaches that have recently been proposed and suggestions for further research related to this field are presented.

Chapter 4 focuses on the impact of electrical faults striking PMSM drives used in automotive applications. Means for providing fault tolerance to inverter faults are discussed in particular. Finally, the impact of electrical faults on a propulsion application is considered and also serves as an introduction to the case studies presented in [Paper VII] and [Paper VIII].

Chapter 5 summarizes the conclusions of the work and provides some proposals for further research.

1.4 Scientific Contributions

In order how they appear in the included papers, the list below summarizes the main contributions presented in this thesis.

- A method for improving the global stability properties of the speed and position estimator in [32] is presented in [Paper I]. The proposed method improves the estimator’s capability to handle large speed estimation errors and is particularly attractive in applications with fast mechanical bandwidth or if a rapid convergence from an initiation at unknown speed is vital.
- The properties of the estimator in [32] when used in the transition region is analyzed in [Paper II] and [Paper III]. It is shown that the estimator may become unstable for certain setups of machine parameters and operating conditions if the estimator parameters are not chosen correctly. To avoid this instability and to maintain proper damping in the whole operation range, design rules for how the transition region

should be determined, as well as recommended selections for all parameters introduced are proposed.

- The global stability properties of an estimator based on the well known “voltage model” are analyzed in [Paper IV] and modifications are proposed in order to improve the estimator’s performance in the low-speed range.
- In [Paper V], the theory of loss minimization, by means of control, is applied to a PMSM drive intended for propulsion in a HEV. The case study, based on simulations, shows that there is little potential to minimize losses by choosing the correct compromise between resistive and core losses due to the additional inverter losses that arise.
- Novel control algorithms for the fault-tolerant PMSM drive proposed in [10] are presented in [Paper VI] in order to allow for closed-loop field weakening control and speed and position estimation also in fault mode. A method for controlling the neutral-point voltage is also presented so that the available voltage capacity of the inverter is maximized in both normal and fault mode.
- The stability of an electric vehicle equipped with in-wheel motors of permanent-magnet type is analyzed in [Paper VII] and [Paper VIII]. It is demonstrated that vehicle stability following an electrical fault can often be maintained with only minor lateral displacements when using a closed-loop path controller. This inherent capacity to handle an important class of electrical faults is attractive; especially since no additional fault-handling strategy is added to the path controller.

1.5 List of Publications

The publications originating from this Ph.D. project are:

- I **O. Wallmark**, L. Harnefors, and O. Carlson, “An improved speed and position estimator for salient permanent-magnet synchronous motors,” *IEEE Transactions on Industrial Electronics*, vol. 52, no. 1, pp. 255-262, Feb. 2005.
- II **O. Wallmark**, L. Harnefors, and O. Carlson, “Sensorless control of PMSM drives for hybrid electric vehicles,” in *Proc. 35th Annual IEEE Power Electronics Specialists Conference (IEEE PESC’04)*, vol. 5, 2004, pp. 4017–4023.
- III **O. Wallmark** and L. Harnefors, “Sensorless control of salient PMSM drives in the transition region,” *IEEE Transactions on Industrial Electronics*, vol. 53, no. 4, pp. 1179-1187, Aug. 2006.

- IV M. Jansson, L. Harnefors, **O. Wallmark**, and M. Leksell, “Synchronization at startup and stable rotation reversal of sensorless nonsalient PMSM drives,” *IEEE Transactions on Industrial Electronics*, vol. 53, no. 2, pp. 379-387, Apr. 2006.
- V **O. Wallmark**, O. Carlson, and L. Harnefors, “Loss minimization of a PMSM drive for a hybrid electric vehicle,” in *Proc. 11th International Conference on Power Electronics and Motion Control (EPE PEMC’04)*, vol. 6, 2004, pp. 160–164.
- VI **O. Wallmark**, L. Harnefors, and O. Carlson, “Control algorithms for a fault-tolerant PMSM drive,” in *Proc. 31st Annual Conference of the IEEE Industrial Electronics Society (IEEE IECON’05)*, 2005, pp. 1467-1473. The slightly revised version included in this thesis is accepted for publication in *IEEE Transactions on Industrial Electronics*.
- VII M. Jonasson and **O. Wallmark**, “Stability of an electric vehicle with permanent-magnet in-wheel motors during electrical faults,” to be presented at the *22nd International Battery, Hybrid and Fuel Cell Electric Vehicle Symposium & Exposition (EVS’22)*.
- VIII M. Jonasson and **O. Wallmark**, “Control of electric vehicles with autonomous corner modules: implementation aspects and fault handling,” submitted to the *International Journal of Vehicle Systems Modelling and Testing*.

[Paper I]–[Paper VIII] are included in this thesis. Prior to this Doctoral thesis, a Licentiate thesis was published [74] including the contributions presented in [Paper I], [Paper II], [Paper V], and [Paper X]. The publications below are related in interest, but not included in this thesis:

- IX **O. Wallmark**, L. Harnefors, and O. Carlson, “Post-fault operation of fault-tolerant inverters for PMSM drives,” in *Proc. 11th European Conference on Power Electronics and Applications (EPE’05)*, 2005.
- X **O. Wallmark**, “Modelling of permanent magnet synchronous machines with non-sinusoidal flux linkage,” in *Proc. Nordic Workshop on Power and Industrial Electronics (NorPIE’02)*, 2002.

1.5.1 Contributions of Individual Authors

As first author, the author of the present thesis has contributed with the major parts in [Paper I]¹–[Paper III], [Paper V], [Paper VI], [Paper IX], and [Paper X]. This includes proposals of fundamental concepts, simulations and experimental evaluations, as well as

¹The fundamental idea of how the estimator considered in this paper could be improved was first coined by Harnefors and was then explored, resulting in [Paper I], by the author of the present thesis.

Chapter 1. Introduction

preparation of the manuscripts. The co-authors have contributed with valuable input in the form of useful ideas and comments, as well as proofreading the manuscripts.

In [Paper IV], the author contributed to the analysis presented in the paper's Section III and Appendix A, as well as commenting and proofreading the manuscript.

In [Paper VII], the contributions from both authors are essentially equal. The author has contributed to all parts of [Paper VII], with the exception of the tire model (Section 3.1) which was made solely by Jonasson. The extension of the vehicle model and force-allocation algorithm adopted in [Paper VIII] were developed by Jonasson and the power electronics simulation was provided by the present author. The remaining parts of the paper were developed jointly.

Chapter 2

Modeling of Permanent-Magnet Synchronous Machines

In this chapter, different aspects of modeling of PMSMs for control purposes are described; see Appendix A for a list of glossary terms. The current and speed controllers used in the various experiments presented in the included papers are also reviewed.

2.1 A PMSM Model Including Spatial Harmonics

Radially magnetized PMSMs are separated into different classes depending on how the rotor magnets are mounted onto (or inside) the rotor. The rotor configuration shown in Fig. 2.1a) adopts *surface-mounted magnets* which are often glued onto the rotor surface. Since the relative permeability of the magnets is almost the same as for air, such a design possesses very small rotor saliency and these are sometimes referred to as “nonsalient” designs. By filling the gaps between the magnets partially with iron, a significant rotor saliency can be achieved which offers the possibility to utilize the reluctance torque. Such an *inset-magnet* design is shown in Fig. 2.1b). The rotor configuration shown in Fig. 2.1c) is an example of an *interior-magnet* design where the rotor magnets are mounted inside the rotor. The placement of the magnets inside the rotor can be made in numerous ways, which offers good opportunities to tailor the level of rotor saliency and magnet flux depending on the application [22].

The fact that three-phase symmetrical sinusoidal quantities are transformed into two dc components through the well known Park transformation has made modeling of PMSMs in the rotor-fixed dq -reference frame used almost exclusively for control purposes. For PMSMs, it is common to align the d axis with the magnetic north pole of the rotor magnet (or an estimation thereof). In the case of multipole machines (n_p is used to denote the number of pole *pairs*), the *electrical* rotor angle θ is used. The q axis is, as exemplified in Fig. 2.1, displaced 90 electrical degrees from the d axis.

The radial flux-density distribution can be expressed using the electrical angle ϑ ,

which is fixed to the d axis. It is evident in Fig. 2.1 that the radial flux-density distribution $B_r(\vartheta)$ must be even around the rotor periphery for all three rotor designs. It is also evident that the “half-wave” condition is met, i.e., $B_r(\vartheta + \pi) = -B_r(\vartheta)$. Hence, $B_r(\vartheta)$ can be expanded into an even Fourier series as

$$B_r(\vartheta) = \sum_{i=1}^{\infty} B_{2i-1} \cos [(2i - 1)\vartheta], \quad (2.1)$$

where the amplitudes of the flux-density harmonics, B_{2i-1} , are strongly dependent on the particular rotor design.

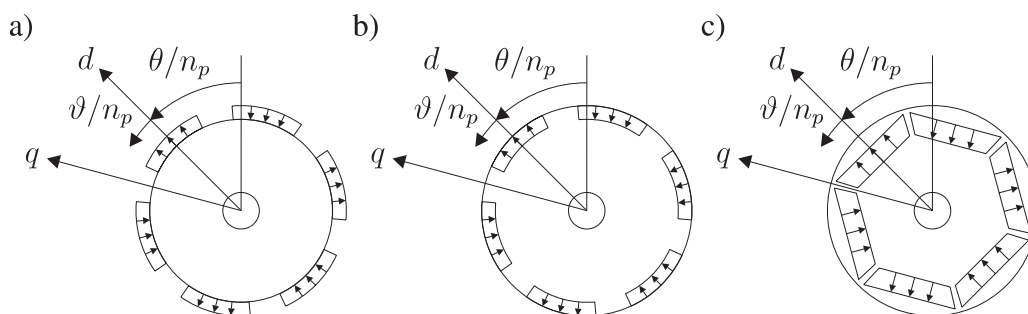


Fig. 2.1 Examples of different rotor magnet designs utilizing three pole pairs: a) Surface-mounted magnets; b) Inset-mounted magnets; c) Interior-mounted magnets.

An example of an ideal, sinusoidally distributed, winding for phase a of a two-pole PMSM is shown in Fig. 2.2 (where the angle ϱ is also defined). Such a winding is hardly realistic in practice and in order to make this derivation more general, it is therefore assumed that the winding distribution $N(\varrho)$ can be expanded into an odd Fourier series as

$$N(\varrho) = \sum_{j=1}^{\infty} N_{2j-1} \sin [(2j - 1)\varrho]. \quad (2.2)$$

Assuming that the flux-density distribution is radial only, the contribution of magnet-flux linkage of the winding at the angle ϱ can now be obtained as [35]

$$d\psi_{m,a} = N(\varrho)d\varrho \int_{-(\varrho+\theta)}^{\varrho-\theta} B_r(\vartheta)r_s l_s d\vartheta, \quad (2.3)$$

where l_s and r_s represent the active length and inner radius of the stator respectively. The total magnet-flux linkage of phase a is now found by integrating along the whole stator periphery,

$$\psi_{m,a}(\theta) = \int_0^{\pi} d\psi_{m,a} = \pi r_s l_s \sum_{i=1}^{\infty} \frac{B_{2i-1} N_{2i-1}}{2i - 1} \cos [(2i - 1)\theta]. \quad (2.4)$$

2.1. A PMSM Model Including Spatial Harmonics

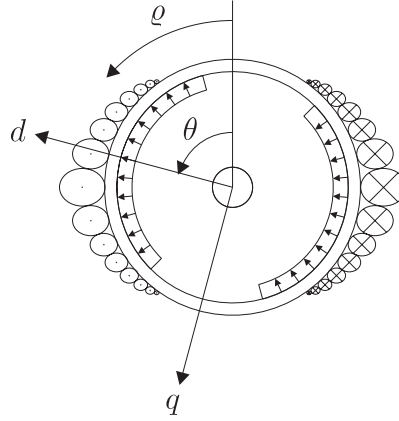


Fig. 2.2 The figure depicts an ideal, sinusoidally distributed winding for a two-pole PMSM. Only the winding for phase a is shown and the phase current is assumed positive.

Eq. (2.4) shows that the magnet-flux linkage can be expressed as a sum of odd cosines, where the amplitude of each harmonic decreases rapidly. Depending on the rotor design, (which affects the flux-density harmonics B_{2i-1}) and the winding distribution (affecting the winding harmonics N_{2i-1}), this filtering property can be altered by the machine designer to suit the specific application. To simplify the notation, (2.4) is now reexpressed as

$$\psi_{m,a}(\theta) \triangleq \sum_{i=1}^{\infty} \psi_{2i-1} \cos [(2i-1)\theta] = \psi_1 \cos \theta + \psi_3 \cos 3\theta + \psi_5 \cos 5\theta + \dots \quad (2.5)$$

The windings for phases b and c are assumed displaced ± 120 electrical degrees relative to phase a . Hence, the magnet-flux linkage for all three phases can be expressed in vector form as

$$\begin{bmatrix} \psi_{m,a}(\theta) \\ \psi_{m,b}(\theta) \\ \psi_{m,c}(\theta) \end{bmatrix} = \begin{bmatrix} \psi_{m,a}(\theta) \\ \psi_{m,a}(\theta - 2\pi/3) \\ \psi_{m,a}(\theta + 2\pi/3) \end{bmatrix} \triangleq \boldsymbol{\psi}_{m,\text{ph}} \quad (2.6)$$

Since the magnetic permeability of the rotor-magnet material is approximately the same as air, the parts of the stator that are aligned to a rotor magnet “sense” a wider air gap, which yields a rotor-angle dependence of the stator-phase inductances. It is evident in Fig. 2.2 that the stator self inductance is the same for both positive and negative rotor angles θ . Hence, the angular dependency of the self inductance for phase a can, at least under nonsaturated conditions, be expressed as

$$L_{s,a}(\theta) = \sum_{i=0}^{\infty} L_{s,2i} \cos (2i\theta) = L_{s,0} + L_{s,2} \cos 2\theta + \dots \quad (2.7)$$

Due to the displacement of the windings for phases b and c , it is evident that $L_{s,b}(\theta) = L_{s,a}(\theta - 2\pi/3)$ and $L_{s,c}(\theta) = L_{s,a}(\theta + 2\pi/3)$. Similarly, the mutual inductance between

phases b and c are found as

$$L_{m,bc}(\theta) = L_{m,cb}(\theta) = \sum_{i=0}^{\infty} L_{m,2i} \cos(2i\theta) = L_{m,0} + L_{m,2} \cos 2\theta + \dots \quad (2.8)$$

Also here, using symmetry arguments, the mutual inductances between the other phases can be expressed as $L_{m,ab}(\theta) = L_{m,ba}(\theta) = L_{m,bc}(\theta + 2\pi/3)$ and $L_{m,ac}(\theta) = L_{m,ca}(\theta) = L_{m,bc}(\theta - 2\pi/3)$. The inductance expressions can now be collected into a symmetric inductance matrix \mathbf{L}_{ph} as

$$\mathbf{L}_{\text{ph}} = \begin{bmatrix} L_{s,a}(\theta) & L_{m,ab}(\theta) & L_{m,ac}(\theta) \\ L_{m,ba}(\theta) & L_{s,b}(\theta) & L_{m,bc}(\theta) \\ L_{m,ca}(\theta) & L_{m,cb}(\theta) & L_{s,c}(\theta) \end{bmatrix}. \quad (2.9)$$

2.1.1 Current Dynamics

Using (2.6) and (2.9), the current dynamics can be expressed in matrix form as

$$\mathbf{v}_{\text{ph},n} = \frac{d}{dt} (\mathbf{L}_{\text{ph}} \mathbf{i}_{\text{ph}} + \boldsymbol{\Psi}_{m,\text{ph}}) + R_s \mathbf{i}_{\text{ph}}, \quad (2.10)$$

where R_s is the resistance of each phase while $\mathbf{v}_{\text{ph},n} = [v_{a,n} \ v_{b,n} \ v_{c,n}]^T$ and $\mathbf{i}_{\text{ph}} = [i_a \ i_b \ i_c]^T$ represent the phase-to-neutral voltages and phase currents respectively. Eq. (2.10) can now be expressed in the rotor-fixed reference frame using the amplitude-invariant Park transformation:

$$\mathbf{T}_{dq,\text{ph}} = \frac{2}{3} \begin{bmatrix} \cos \theta & \cos(\theta - 2\pi/3) & \cos(\theta + 2\pi/3) \\ -\sin \theta & -\sin(\theta - 2\pi/3) & -\sin(\theta + 2\pi/3) \\ 1/2 & 1/2 & 1/2 \end{bmatrix}. \quad (2.11)$$

Hence, the three-phase components f_a , f_b , and f_c , which can represent either currents or voltages, are transformed into $dq0$ -quantities as $[f_d \ f_q \ f_0]^T = \mathbf{T}_{dq,\text{ph}} [f_a \ f_b \ f_c]^T$, where f_0 represents the zero-sequence component. This results in

$$\mathbf{v}_{dq0} = \mathbf{T}_{dq,\text{ph}} \frac{d}{dt} \left(\mathbf{L}_{\text{ph}} \mathbf{T}_{dq,\text{ph}}^{-1} \mathbf{i}_{dq0} + \boldsymbol{\Psi}_{m,\text{ph}} \right) + R_s \mathbf{i}_{dq0}, \quad (2.12)$$

where $\mathbf{v}_{dq0} = [v_d \ v_q \ v_0]^T$ and $\mathbf{i}_{dq0} = [i_d \ i_q \ i_0]^T$. For balanced operation, the zero-sequence components can be neglected¹ (the zero-sequence current is identically zero and a zero-sequence voltage component does not affect the phase currents). Using this simplification, (2.12) can be reexpressed as

$$\mathbf{v}_{dq} = \mathbf{L}_{dq} \frac{d\mathbf{i}_{dq}}{dt} + \mathbf{Z}_{dq} \mathbf{i}_{dq} + \omega_r \boldsymbol{\Psi}_{m,dq}, \quad (2.13)$$

¹This assumption is not valid for the fault-tolerant PMSM drive for which control algorithms are presented in [Paper VI] and [Paper IX], i.e., the zero-sequence components must be taken into account.

2.1. A PMSM Model Including Spatial Harmonics

where $\mathbf{v}_{dq} = [v_d \ v_q]^T$, $\mathbf{i}_{dq} = [i_d \ i_q]^T$, and $\boldsymbol{\Psi}_{m,dq}$ is found as

$$\boldsymbol{\Psi}_{m,dq} = \begin{bmatrix} \sum_{i=1}^{\infty} \psi_{d,6i} \sin(6i\theta) \\ \psi_m + \sum_{i=0}^{\infty} \psi_{q,6i} \cos(6i\theta) \end{bmatrix}. \quad (2.14)$$

In (2.14), $\psi_m = \psi_1$ and $\psi_{d,6i}$ and $\psi_{q,6i}$ are related to (2.5) as

$$\psi_{d,6i} = -(6i - 1)\psi_{6i-1} - (6i + 1)\psi_{6i+1}, \quad i = 1, 2, \dots \quad (2.15a)$$

$$\psi_{q,6i} = -(6i - 1)\psi_{6i-1} + (6i + 1)\psi_{6i+1}, \quad i = 1, 2, \dots \quad (2.15b)$$

Finally, \mathbf{L}_{dq} and \mathbf{Z}_{dq} can be expressed as

$$\mathbf{L}_{dq} = \begin{bmatrix} \sum_{i=0}^{\infty} L_{6i,1} \cos(6i\theta) & \sum_{i=1}^{\infty} L_{6i,2} \sin(6i\theta) \\ \sum_{i=1}^{\infty} L_{6i,3} \sin(6i\theta) & \sum_{i=0}^{\infty} L_{6i,4} \cos(6i\theta) \end{bmatrix}, \quad (2.16)$$

$$\mathbf{Z}_{dq} = \begin{bmatrix} R_s - \omega_r \sum_{i=1}^{\infty} L_{6i,5} \sin(6i\theta) & -\omega_r \sum_{i=0}^{\infty} L_{6i,6} \cos(6i\theta) \\ \omega_r \sum_{i=0}^{\infty} L_{6i,7} \cos(6i\theta) & R_s + \omega_r \sum_{i=1}^{\infty} L_{6i,8} \sin(6i\theta) \end{bmatrix}. \quad (2.17)$$

The general expressions governing how $L_{6i,1}$, $L_{6i,2}$, \dots , $L_{6i,8}$ are related to the components in (2.9) are, due to their complexity, omitted here. However, if only inductance harmonics up to the fourth order are taken into account, \mathbf{L}_{dq} and \mathbf{Z}_{dq} reduce to

$$\mathbf{L}_{dq} = \begin{bmatrix} L_d + \frac{L_6}{5} \cos 6\theta & -\frac{L_6}{5} \sin 6\theta \\ -\frac{L_6}{5} \sin 6\theta & L_q - \frac{L_6}{5} \cos 6\theta \end{bmatrix}, \quad (2.18)$$

$$\mathbf{Z}_{dq} = \begin{bmatrix} R_s - \omega_r L_6 \sin 6\theta & -\omega_r L_q - \omega_r L_6 \cos 6\theta \\ \omega_r L_d - \omega_r L_6 \cos 6\theta & R_s + \omega_r L_6 \sin 6\theta \end{bmatrix}, \quad (2.19)$$

where the notation

$$L_d = L_{s,0} + L_{s,2}/2 - L_{m,0} + L_{m,2}, \quad (2.20a)$$

$$L_q = L_{s,0} - L_{s,2}/2 - L_{m,0} - L_{m,2}, \quad (2.20b)$$

$$L_6 = 5 \left(\frac{L_{s,4}}{2} + L_{m,4} \right), \quad (2.20c)$$

is introduced. If *all* harmonics (in terms of magnet-flux linkage and inductance variation) are neglected, the current dynamics simplify to

$$v_d = R_s i_d + L_d \frac{di_d}{dt} - \omega_r L_q i_q, \quad (2.21)$$

$$v_q = R_s i_q + L_q \frac{di_q}{dt} + \omega_r L_d i_d + \omega_r \psi_m, \quad (2.22)$$

which is the standard model (for control purposes) of the current dynamics for a salient PMSM. For PMSMs with negligible rotor saliency, the d - and q -axis inductances are equal, i.e., $L_d = L_q = L_{s,0} - L_{m,0} \triangleq L_s$. The model consisting of (2.13), (2.18), and (2.19) was adopted in [Paper II] and [Paper III] in order to obtain better agreement with the experimental results than what was predicted using (2.21) and (2.22) (see, e.g., Fig. 9 and Fig. 10 in [Paper III]).

2.1.2 Electromagnetic Torque

Assuming linear magnetic conditions, the magnetic coenergy W_{co} can, in three-phase quantities, be expressed as [48]

$$W_{\text{co}} = \frac{1}{2} \mathbf{i}_{\text{ph}}^T \mathbf{L}_{\text{ph}} \mathbf{i}_{\text{ph}} + \mathbf{i}_{\text{ph}}^T \boldsymbol{\Psi}_{m,\text{ph}}. \quad (2.23)$$

Hence, the electromagnetic torque expression, found by differentiating the magnetic coenergy with respect to the mechanical rotor position θ_{mech} is found as

$$T_e(\theta) = \frac{\partial W_{\text{co}}}{\partial \theta_{\text{mech}}} = n_p \frac{\partial W_{\text{co}}}{\partial \theta} = n_p \left(\frac{1}{2} \mathbf{i}_{\text{ph}}^T \frac{\partial \mathbf{L}_{\text{ph}}}{\partial \theta} \mathbf{i}_{\text{ph}} + \mathbf{i}_{\text{ph}}^T \frac{\partial \boldsymbol{\Psi}_{m,\text{ph}}}{\partial \theta} \right). \quad (2.24)$$

Using (2.11), the electromagnetic torque can be expressed in $dq0$ -quantities which yields

$$T_e(\theta) = n_p \left[\frac{1}{2} \left(\mathbf{T}_{dq,\text{ph}}^{-1} \mathbf{i}_{dq0} \right)^T \frac{\partial \mathbf{L}_{\text{ph}}}{\partial \theta} \mathbf{T}_{dq,\text{ph}}^{-1} \mathbf{i}_{dq0} + \left(\mathbf{T}_{dq,\text{ph}}^{-1} \mathbf{i}_{dq0} \right)^T \frac{\partial \boldsymbol{\Psi}_{m,\text{ph}}}{\partial \theta} \right]. \quad (2.25)$$

Introducing $\Delta L = L_q - L_d$, neglecting the zero-sequence components, and truncating (2.25) to contain inductance harmonics up to the sixth order and magnet-flux linkage harmonics up to order 12, (2.25) simplifies to

$$T_e(\theta) = \frac{3n_p}{2} \left[\psi_m i_q - \Delta L i_d i_q - \frac{2}{5} L_6 \left((i_q^2 - i_d^2) \sin 6\theta + 2i_d i_q \cos 6\theta \right) + i_d (\psi_{d,6} \sin 6\theta + \psi_{d,12} \sin 12\theta) + i_q (\psi_{q,6} \cos 6\theta + \psi_{q,12} \cos 12\theta) \right]. \quad (2.26)$$

As seen in (2.26), apart from the magnet- and reluctance-torque components, i.e., $\psi_m i_q$ and $\Delta L i_d i_q$, both magnet-flux linkage and inductance harmonics are sources of torque ripple.

An additional source of torque ripple is known as *cogging torque*, which is generated by the interaction of magnet flux from the rotor and the angular variation in the magnetic reluctance of the stator. Since this torque component produces no stator excitation, it is not found in the torque expression given by (2.26).

2.2 Core Losses

Core losses, caused by eddy currents and the hysteresis effect, arise in both the stator and rotor cores as well as in the rotor magnets [26]. An accurate prediction of these losses is important for the machine designer in order to enable high-efficient machine designs.

The introduction of modern DSPs has made the implementation of advanced control algorithms for electric drives possible. Hence, the possibility to reduce the *total* losses, including parts of the core losses, through control action has been investigated by several researchers; recent references include [16], [68], [51], [46]. The fundamental idea is to reduce the core losses in the stator by adding additional field weakening (which is achieved by selecting $i_d < 0$). The additional field weakening increases the resistive losses and it is assumed that an optimal set of currents (in terms of i_d and i_q) exists that minimizes the total losses at each operating point (in terms of torque and speed). The core losses that can be affected through control action are typically modeled using equivalent *core-loss resistances*, R_c , as shown in Fig. 2.3.

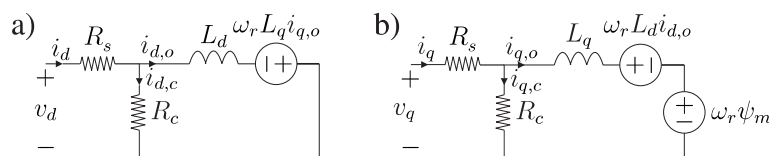


Fig. 2.3 A PMSM model taking core losses into account: a) d axis; b) q axis.

Naturally, the parameters in the circuits shown in Fig. 2.3 must be known accurately. However, they are all prone to variation depending on the current operating point. Nevertheless, the approach has been experimentally demonstrated to successfully reduce losses compared to the well known *maximum torque-per-ampere* (MTPA) control strategy [51].

In [Paper V], a case study is presented that investigates the extent to which this approach is beneficial for an experimental PMSM² developed for propulsion in a series HEV. The approach is attractive since the losses are reduced while no additional hardware is added to the system. However, the case study shows that the additional inverter losses, due to the extra field weakening added, reduce the potential to minimize losses considerably, i.e., the MTPA control strategy is near optimal for the specific PMSM drive. This further enlightens that the impact of losses in both power electronics and electric machines should be considered jointly when designing electric drive systems for EVs and HEVs.

²More details concerning the PMSM can be found in Appendix B where it is referred to as PMSM1.

2.3 Field-Weakening Operation

For operation above base speed, the induced *electromotive force* (EMF) exceeds the available inverter voltage, and field-weakening must be adopted by selecting $i_d < 0$. In the current dq -plane, the current limit manifests itself as a circle with a radius of 1 per unit³ (pu). For nonsalient PMSMs, the voltage limit, when neglecting the resistive voltage drop, also manifests itself as a circle, centered around $i_d = -\psi_m/L_s$ and $i_q = 0$. Whereas for salient PMSMs, an ellipse is formed. Including the resistive voltage drop results in an anti-clockwise rotation of the voltage-limit area. Furthermore, taking into account the saturation of L_q causes the voltage-limit area to increase in the vertical direction [73]. Fig 2.4 shows the available operation regions for PMSM1 and PMSM2⁴ at three different rotor speeds.

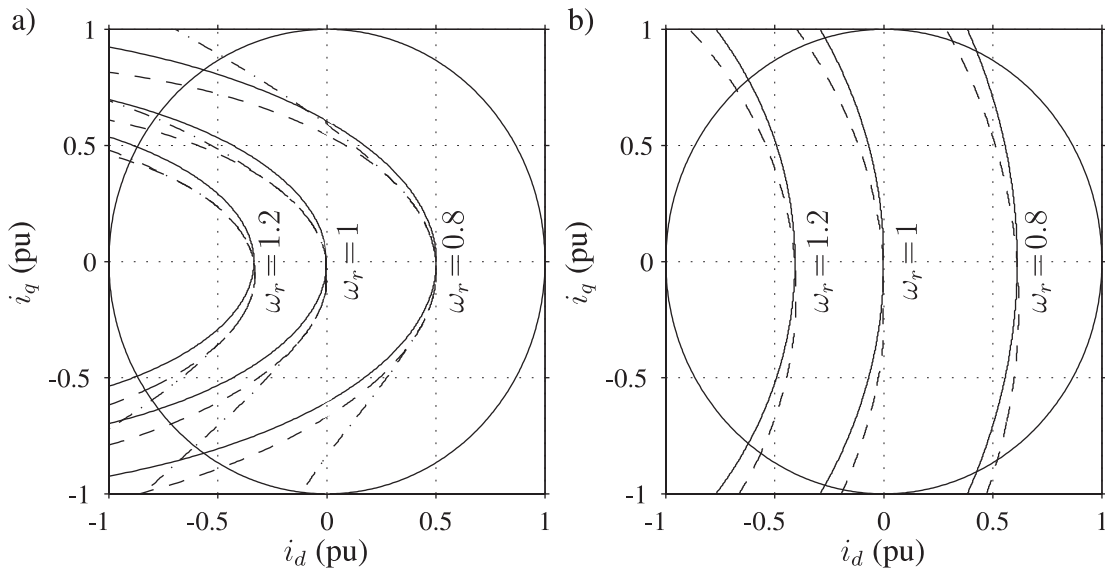


Fig. 2.4 Available operation regions, expressed in the current dq -plane for three rotor speeds $\omega_r = \{0.8, 1, 1.2\}$ pu for: a) PMSM1 and b) PMSM2. Solid lines represent the current-limit circle (constant) and voltage limits (varying with speed) where the resistive voltage drop has been neglected. Dashed lines represent the voltage limits when the resistive voltage drop is included. Dashed-dotted lines (only for PMSM1) represent the voltage limit including the resistive voltage drop and the effect of saturation on L_q .

In [Paper VI] (see also Fig. 2.5), operation in the field-weakening region is achieved by controlling i_d^{ref} using a variant of the closed-loop field-weakening controller presented in [47], with the modifications found in [33]. The algorithm is further analyzed in the Licentiate thesis [74].

³See Appendix B for a definition of the per-unit system adopted in the present thesis.

⁴More details concerning the PMSM referred to as PMSM2 can be found in Appendix B.

2.4 Current and Speed Control

A significant part of the contributions presented in this thesis focus on how to obtain accurate speed and position estimates using information found in the phase currents and inverter voltages. These estimates replace their corresponding measured states and are used in conjunction with closed-loop speed and current controllers. The speed and current controllers used in the various experiments are therefore briefly reviewed here.

2.4.1 Current Control

The current controller reviewed here was, in this form, presented in [33], using the concept of *internal model control* (IMC). For a nonsalient PMSM, the controller can be expressed as

$$v_d^{\text{ref}} = k_p (i_d^{\text{ref}} - i_d) + k_i I_d - \omega_r \hat{L}_s i_q - R_a i_d, \quad (2.27)$$

$$v_q^{\text{ref}} = k_p (i_q^{\text{ref}} - i_q) + k_i I_q + \omega_r \hat{L}_s i_d - R_a i_q. \quad (2.28)$$

The first two terms on the right-hand sides of (2.27) and (2.28) represent standard PI controllers (I_d and I_q represent the integrator states). Since (2.21) and (2.22) are coupled, the third terms on the right-hand sides of (2.27) and (2.28) are added for decoupling purposes. The last terms are called *active damping* (named *active resistance* in [13]) and are added in order to reduce the impact of $\omega_r \psi_m$ which acts as a disturbance in (2.22). The parameters of the controller are selected as in [33]

$$k_p = \alpha_c \hat{L}_s, \quad k_i = \alpha_c k_p, \quad R_a = \alpha_c \hat{L}_s - \hat{R}_s, \quad (2.29)$$

where α_c is the desired bandwidth of the closed-loop system and “hats” indicate model parameters. By substituting (2.27) and (2.28) in (2.21) and (2.22), and noting that $\dot{I}_d = i_d^{\text{ref}} - i_d$ and $\dot{I}_q = i_q^{\text{ref}} - i_q$, a fourth-order, linear system is formed. Selecting the state vector as $\mathbf{x} = [i_d \ i_q \ I_d \ I_q]^T$, the disturbance as $\boldsymbol{\nu} = [\omega_r]$, and the input as $\mathbf{u} = [i_d^{\text{ref}} \ i_q^{\text{ref}}]^T$, the system can be expressed in state-space form as $\dot{\mathbf{x}} = \mathbf{A}\mathbf{x} + \mathbf{B}\mathbf{u} + \mathbf{E}\boldsymbol{\nu}$. Neglecting parameter errors, the expressions for \mathbf{A} , \mathbf{B} , and \mathbf{E} are found as

$$\mathbf{A} = \begin{bmatrix} -2\alpha_c & 0 & \alpha_c^2 & 0 \\ 0 & -2\alpha_c & 0 & \alpha_c^2 \\ -1 & 0 & 0 & 0 \\ 0 & -1 & 0 & 0 \end{bmatrix}, \quad \mathbf{B} = \begin{bmatrix} \alpha_c & 0 \\ 0 & \alpha_c \\ 1 & 0 \\ 0 & 1 \end{bmatrix}, \quad \mathbf{E} = \begin{bmatrix} 0 \\ -\psi_m/L_s \\ 0 \\ 0 \end{bmatrix}. \quad (2.30)$$

Introducing p as the derivative operator, i.e., $p = d/dt$, the system can be expressed in operator form as

$$\mathbf{x}(p) = \underbrace{(p\mathbf{I} - \mathbf{A})^{-1} \mathbf{B}}_{\mathbf{G}(p)} \mathbf{u}(p) + \underbrace{(p\mathbf{I} - \mathbf{A})^{-1} \mathbf{E}}_{\mathbf{S}(p)} \boldsymbol{\nu}(p), \quad (2.31)$$

where $\mathbf{G}(p)$ and $\mathbf{S}(p)$ represent the closed-loop dynamics and the sensitivity function, respectively (their full forms are omitted here). From (2.31), the following relations are obtained

$$i_d(p) = \underbrace{\frac{\alpha_c}{p + \alpha_c}}_{G_{cl}(p)} i_d^{\text{ref}}(p), \quad (2.32)$$

$$i_q(p) = \underbrace{\frac{\alpha_c}{p + \alpha_c}}_{G_{cl}(p)} i_q^{\text{ref}}(p) + \underbrace{\frac{-p\psi_m}{L_s(p + \alpha_c)^2}}_{S(p)} \omega_r(p). \quad (2.33)$$

The closed-loop current dynamics $G_{cl}(p)$ consist of two, decoupled, first-order systems. As is well known, the rise time t_r of a first-order system is related to the bandwidth α as $t_r = \ln 9/\alpha$. Hence, the controller is parameterized into machine parameters and the desired bandwidth. This is attractive since it simplifies the implementation considerably as the tuning procedure of the controller is simplified (removed). In (2.33), $S(p)$ represents the controller's sensitivity to the disturbance $\omega_r(p)$. As can be seen, $S(p)$ has two poles at $p = -\alpha_c$, i.e., it is as fast as the closed-loop dynamics whose pole also is located at $p = -\alpha_c$. The dynamics of the current control loop can be made very fast in relation to its mechanical counterpart. Even when using a moderate inverter switching frequency of, for instance, a few kHz, the closed-loop current dynamics, governed by α_c , can easily be selected to obtain rise times in the range of a few milliseconds or even faster.

2.4.2 Speed Control

The speed controller presented in [33] computes its output in the form of a torque reference as

$$T_e^{\text{ref}} = k_p (\omega_r^{\text{ref}} - \omega_r) + k_i I_s - b_a \omega_r, \quad (2.34)$$

where k_p and k_i are the PI controller parameters (I_s represents the integrator state) and b_a is an active damping gain. Assuming a nonsalient PMSM, the d - and q -current references are, from (2.34), computed as

$$i_d^{\text{ref}} = 0, \quad i_q^{\text{ref}} = \frac{2T_e^{\text{ref}}}{3n_p \hat{\psi}_m}, \quad (2.35)$$

in order to obtain the desired torque with minimum resistive losses. The closed-loop speed control can now, in state-space form, be expressed as

$$J\dot{\omega}_r = n_p (T_e^{\text{ref}} - T_l) - b_{\text{fric}}\omega_r, \quad (2.36)$$

$$\dot{I}_s = \omega_r^{\text{ref}} - \omega_r, \quad (2.37)$$

where J is the inertia, T_l is the load torque, and b_{fric} represents the viscous friction torque. The parameters of the speed controller are chosen as [33]

$$k_p = b_a = \frac{\alpha_s \hat{J}}{n_p}, \quad k_i = \alpha_s k_p, \quad (2.38)$$

where α_s is the desired bandwidth of the speed control loop. Substituting (2.38) in (2.36) and (2.37), and using the reasonable assumption $\alpha_s J \gg b_{\text{fric}}$, the following state-space system is formed

$$\underbrace{\begin{bmatrix} \dot{\omega}_r \\ \dot{I}_s \end{bmatrix}}_{\dot{\mathbf{x}}} = \underbrace{\begin{bmatrix} -2\alpha_s & \alpha_s^2 \\ -1 & 0 \end{bmatrix}}_{\mathbf{A}} \underbrace{\begin{bmatrix} \omega_r \\ I_s \end{bmatrix}}_{\mathbf{x}} + \underbrace{\begin{bmatrix} 0 \\ -\frac{n_p}{J} \end{bmatrix}}_{\mathbf{B}} \underbrace{\begin{bmatrix} \omega_r^{\text{ref}} \end{bmatrix}}_{\mathbf{u}} + \underbrace{\begin{bmatrix} 1 \\ \alpha_s \end{bmatrix}}_{\mathbf{E}} \underbrace{\begin{bmatrix} T_l \end{bmatrix}}_{\boldsymbol{\nu}}, \quad (2.39)$$

where parameter errors have been neglected. As in (2.31), the system can be expressed in operator form as

$$\mathbf{x}(p) = \underbrace{(p\mathbf{I} - \mathbf{A})^{-1} \mathbf{B}}_{\mathbf{G}(p)} \mathbf{u}(p) + \underbrace{(p\mathbf{I} - \mathbf{A})^{-1} \mathbf{E}}_{\mathbf{S}(p)} \boldsymbol{\nu}(p). \quad (2.40)$$

From (2.40), the following relation is obtained

$$\omega_r(p) = \underbrace{\frac{\alpha_s}{p + \alpha_s}}_{G_{\text{cl}}(p)} \omega_r^{\text{ref}}(p) + \underbrace{\frac{-n_p p}{J(p + \alpha_s)^2}}_{S(p)} T_l(p). \quad (2.41)$$

Similar to (2.33), the closed-loop dynamics consist of a first-order system governed by the bandwidth α_s , and, because of the active damping, the sensitivity to the load-torque disturbance T_l can be made as fast as the closed-loop system. The speed controller relies on the assumption that the current dynamics are fast and can be neglected. Hence, the condition $\alpha_s \ll \alpha_c$ must be fulfilled for proper operation.

2.4.3 Experimental Evaluation

Adopting closed-loop current controllers of the PI-type (implemented in the rotor-fixed reference frame) and closing an outer loop for speed control has been proven very successful and is often the meaning of the term *vector control* when it is applied to PMSM drives. In order to complete the review of the current and speed controllers discussed above, an experimental step response in speed is presented in Fig. 2.5 using a PMSM of outer-rotor type (referred to in Appendix B as PMSM2). The current and speed control loops are selected to obtain 10%–90% rise times of approximately 2 ms and 0.4 s, respectively, i.e., $\alpha_c = \ln 9/2 \cdot 10^{-3} \approx 1100$ rad/s and $\alpha_s = \ln 9/0.4 \approx 5.5$ rad/s. A dc-link voltage

of 150 V is used in the experiment, and therefore, the implemented closed-loop field-weakening controller automatically reduces i_d as the speed increases in order to avoid voltage saturation.

The experimentally obtained rise times in current and speed are 2 ms and 0.3 s, respectively, which correlate quite well with the desired rise times. The fact that the experimentally obtained rise time in speed is somewhat shorter than desired is likely due to a mismatch of the inertia J , which introduces slight errors into the PI gains of the speed controller.

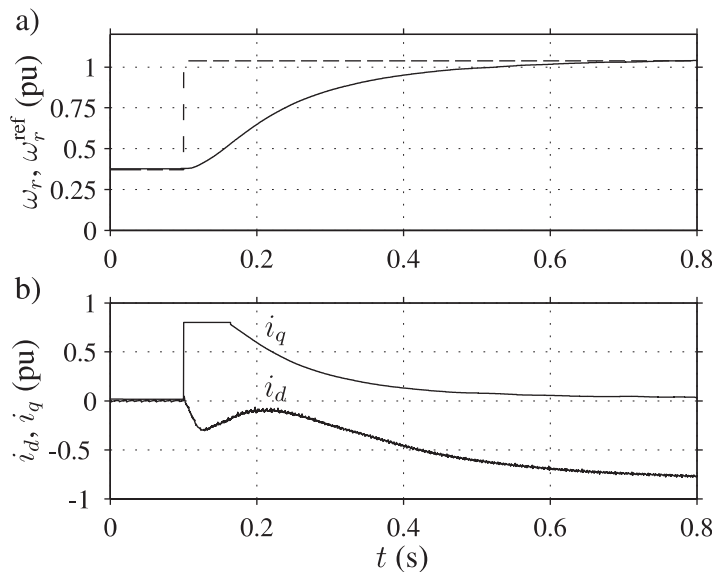


Fig. 2.5 Experimental speed step response using PMSM2.

2.5 Summary of Chapter

This chapter has discussed different aspects of modeling of PMSMs for control purposes. The intention was mainly to provide a background and introduce the notation used in the following chapters and included papers. The dynamic PMSM model, including the effect of spatial harmonics, constitutes the current dynamics governed by (2.12), and the electromagnetic torque expression, (2.25). The orders of the spatial harmonics were determined solely by arguments of symmetry; a more detailed derivation can be found in [11].

The algorithms for speed and position estimation, discussed in Chapter 3 and the included papers, are used in conjunction with closed-loop speed and current controllers. Therefore, the speed and current controllers used in the various experiments were also briefly reviewed; a more detailed review, which also considers closed-loop field-weakening control, is presented in the Licentiate thesis [74].

Chapter 3

Speed and Position Estimation

This chapter considers rotor position and speed estimation, i.e., sensorless control, of PMSMs. A phase-locked loop (PLL) type estimator previously reported in the literature is analyzed and improvements, presented further in the included papers, are proposed. Finally, a review of developments and approaches that have been recently proposed is presented.

3.1 Introduction

As is well known, there are, in principle, two different methods of obtaining estimates of speed and rotor position in a vector controlled PMSM.

In the first category, information is obtained from the back EMF. Such type of estimators show good performance in the medium and high speed regions. However, since the back EMF vanishes at low speeds, low and zero speed operation is challenging. The number of contributions concerning operation at speeds above the low-speed range is vast; references [1] and [67] present recent overviews of different methods (belonging to both the first and second categories) presented in the literature.

In the second category, a high-frequency carrier signal is added and information is obtained provided that the machine possesses rotor anisotropy, i.e., saliency. The algorithms proposed are typically variants of the high-frequency signal-injection method presented in [19] or what is referred to as the “INFORM” method¹ [66]. Although these techniques allow for zero- and low-speed operation, obvious drawbacks are that they, at least to some extent, lead to acoustic noise, torque ripple, and increased losses. If the PMSM possesses saliency, a combination of the two categories is typically used, where high-frequency signal injection methods are relied on at low speeds and a transition to back-EMF estimation methods is performed at higher speeds.

¹The term INFORM is an abbreviation for INdirect Flux detection by On-line Reactance Measurement.

3.1.1 Automotive Applications

It is obvious that cost-, size-, and reliability-related benefits, gained by removing the rotor position sensor, are of interest for the automotive industry. Several different applications exist in a vehicle where sensorless drives can be attractive. These applications include propulsion [69], [52], [24], [20], automotive steering [5], and automotive air compressors [60].

In several of these applications, the PMSM operates at all speeds (including zero speed). Only very small steady-state position estimation errors are allowed, operation deep into the field-weakening region can be expected, and stable operation at all possible operating points must be guaranteed. Naturally, these demands can be fulfilled by accurately tuning a specific estimator, used in conjunction with a specific drive. However, to support results obtained from measurements, analysis of the algorithms should be carried out to better understand their properties in different modes of operation. Preferably, to simplify an implementation, design guidelines for all parameters introduced should also be presented. Several of the scientific contributions presented in this thesis concerning sensorless PMSM drives are essentially design guidelines that are obtained from a thorough analysis of the algorithms in consideration.

3.1.2 Outline of Chapter

As mentioned in Chapter 1, the main focus concerning speed and position estimation in this thesis is not to present an entirely novel type of estimator but rather point out and present solutions for different problems associated with promising estimation methods previously reported in the literature. Since the methods of analysis are often general, the results should also be applicable to and provide insight into other candidate estimators.

This chapter serves as an introduction to the included papers concerning speed and position estimation and is outlined as follows. Section 3.2 provides a brief introduction to an estimator of PLL type that has been previously reported in the literature. The analysis presented also demonstrates two general problems associated with speed and position estimation for PMSM drives, as well as highlighting some issues concerning the specific estimator. Finally, Section 3.3 presents a review of developments and approaches that have been recently presented in the literature.

3.2 Some Properties of a PLL-Type Estimator

In [Paper I]–[Paper III], [Paper VI], and [Paper IX], improvements for a speed and position estimator whose dynamics correspond to a PLL are proposed. The original version of the estimator was proposed in [32]. To simplify for the reader, as well as to demonstrate some properties not extensively covered in [32] or the included papers, an introductory

3.2. Some Properties of a PLL-Type Estimator

analysis of this PLL-type estimator is presented here.

As shown in Chapter 2, the current dynamics are governed by (2.13), which is here restated as

$$\mathbf{v}_{dq} = \mathbf{L}_{dq} \frac{d\mathbf{i}_{dq}}{dt} + \mathbf{Z}_{dq} \mathbf{i}_{dq} + \omega_r \boldsymbol{\psi}_{m,dq}. \quad (3.1)$$

To simplify the mathematical details in the present discussion, a nonsalient PMSM is considered and all spatial harmonics are neglected, i.e., $\mathbf{L}_{dq} = \text{diag}(L_s, L_s)$, $\boldsymbol{\psi}_{m,dq} = [0 \ \omega_r \psi_m]^T$, and

$$\mathbf{Z}_{dq} = \begin{bmatrix} R_s & -\omega_r L_s \\ \omega_r L_s & R_s \end{bmatrix}. \quad (3.2)$$

Now, an *estimated reference frame* is introduced, displaced by the angle $\tilde{\theta} = \theta - \hat{\theta}$. The rotor-fixed and estimated reference frames are shown in Fig. 3.1. The transformation of a general current or voltage vector, $\mathbf{f} = [f_d \ f_q]^T$, is governed by $\hat{\mathbf{f}} = e^{\mathbf{J}\tilde{\theta}} \mathbf{f}$, where $\hat{\mathbf{f}} = [\hat{f}_d \ \hat{f}_q]^T$. Here, the matrices \mathbf{J} and $e^{\mathbf{J}\tilde{\theta}}$ are introduced as

$$e^{\mathbf{J}\tilde{\theta}} = \begin{bmatrix} \cos \tilde{\theta} & -\sin \tilde{\theta} \\ \sin \tilde{\theta} & \cos \tilde{\theta} \end{bmatrix}, \quad \mathbf{J} = \begin{bmatrix} 0 & -1 \\ 1 & 0 \end{bmatrix}. \quad (3.3)$$

Using (3.3), (3.1) can now be expressed in the estimated reference frame as

$$\hat{\mathbf{v}}_{dq} = e^{\mathbf{J}\tilde{\theta}} \mathbf{L}_{dq} e^{-\mathbf{J}\tilde{\theta}} \frac{d\hat{\mathbf{i}}_{dq}}{dt} - e^{\mathbf{J}\tilde{\theta}} \mathbf{L}_{dq} \mathbf{J} \tilde{\omega}_r e^{-\mathbf{J}\tilde{\theta}} \hat{\mathbf{i}}_{dq} + e^{\mathbf{J}\tilde{\theta}} \mathbf{Z}_{dq} e^{-\mathbf{J}\tilde{\theta}} \hat{\mathbf{i}}_{dq} + e^{\mathbf{J}\tilde{\theta}} \omega_r \boldsymbol{\psi}_{m,dq}. \quad (3.4)$$

An error vector, $\hat{\mathbf{e}} = [e_{\hat{d}} \ e_{\hat{q}}]^T$, containing information about the true rotor position is now obtained by subtracting the resistive and rotational voltage drops from $\hat{\mathbf{v}}_{dq}$:

$$\hat{\mathbf{e}} = \hat{\mathbf{v}}_{dq} - \hat{\mathbf{Z}} \hat{\mathbf{i}}_{dq}, \quad \hat{\mathbf{Z}} = \begin{bmatrix} \hat{R}_s & -\hat{\omega}_r \hat{L}_s \\ \hat{\omega}_r \hat{L}_s & \hat{R}_s \end{bmatrix}, \quad (3.5)$$

where \hat{R}_s and \hat{L}_s denote model (estimated) machine parameters, and the (unknown) rotor speed is replaced with its estimate. Assuming no parameter errors, $e_{\hat{d}}$ and $e_{\hat{q}}$ are found to be

$$e_{\hat{d}} = L_s \frac{di_{\hat{d}}}{dt} - \omega_r \psi_m \sin \tilde{\theta}, \quad e_{\hat{q}} = L_s \frac{di_{\hat{q}}}{dt} + \omega_r \psi_m \cos \tilde{\theta}. \quad (3.6)$$

If the bandwidth of the estimator is considerably lower than the bandwidth of the closed-loop current dynamics (governed by α_c , see Section 2.4.1), the current dynamics can safely be neglected, i.e., $di_{\hat{d}}/dt = di_{\hat{q}}/dt = 0$ can be assumed, and $e_{\hat{d}}$ and $e_{\hat{q}}$ simplify to

$$e_{\hat{d}} = -\omega_r \psi_m \sin \tilde{\theta}, \quad e_{\hat{q}} = \omega_r \psi_m \cos \tilde{\theta}. \quad (3.7)$$

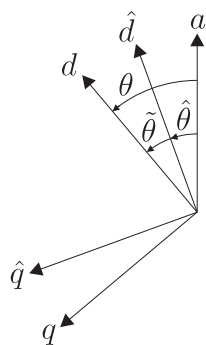


Fig. 3.1 Definition of the rotor-fixed dq -reference frame and its estimate.

The position information found in (3.7) can be used to design back-EMF based speed and position estimators with different properties in terms of dynamics and estimation accuracy. The PLL-type estimator in [32] uses only $e_{\hat{d}}$ for estimation purposes and the speed and position estimates are updated as

$$\dot{\hat{\omega}}_r = -\gamma_1 e_{\hat{d}}, \quad (3.8)$$

$$\dot{\hat{\theta}} = \hat{\omega}_r - \gamma_2 e_{\hat{d}}, \quad (3.9)$$

where γ_1 and γ_2 are gain parameters which are chosen as

$$\gamma_1 = \begin{cases} \rho^2 / (\hat{\omega}_r \hat{\psi}_m), & |\hat{\omega}_r| \geq \omega_\Delta \\ \hat{\omega}_r \rho^2 / (\omega_\Delta \hat{\psi}_m), & |\hat{\omega}_r| < \omega_\Delta \end{cases} \quad (3.10)$$

$$\gamma_2 = \begin{cases} 2\rho / (\hat{\omega}_r \hat{\psi}_m), & |\hat{\omega}_r| \geq \omega_\Delta \\ 2 \operatorname{sign}(\hat{\omega}_r) \rho / (\omega_\Delta \hat{\psi}_m), & |\hat{\omega}_r| < \omega_\Delta. \end{cases} \quad (3.11)$$

In (3.10) and (3.11), ρ represents the bandwidth of the estimator. As seen, the gains γ_1 and γ_2 are inversely proportional to the (estimated) rotor speed at nominal speeds, i.e., for $|\hat{\omega}_r| \geq \omega_\Delta$. In order to avoid excessive gains at low speeds, γ_1 and γ_2 are chosen differently for $|\hat{\omega}_r| < \omega_\Delta$, which, as will be shown below, also results in worsened dynamics. A flowchart of the algorithm is shown in Fig. 3.2.

3.2.1 Experimental Evaluation

For purposes of demonstration, Fig. 3.3 shows an experimental step response in speed with experimental conditions identical to Section 2.4.3 with the exception of speed and rotor position, which are estimated using the PLL-type estimator, whose bandwidth is chosen as $\rho = \alpha_c / 20$. As seen, the rotor position is accurately estimated; $\tilde{\theta}$ is smaller than 10 (electrical) degrees during the transient and only a couple of degrees in the steady state.

3.2. Some Properties of a PLL-Type Estimator

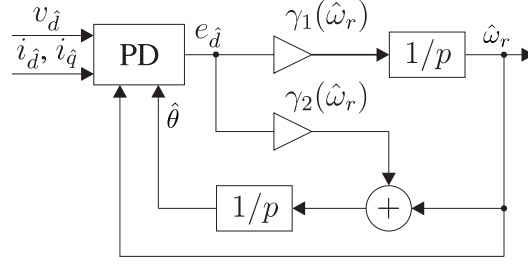


Fig. 3.2 Flowchart of the PLL-type estimator presented in [32]. The PD block, corresponding to the phase detector of a standard PLL, contains coordinate transformations using $\hat{\theta}$ and computation of the error signal $e_{\hat{d}}$.

3.2.2 Linearized Error Dynamics

The speed and position estimation *errors* are now introduced as $\tilde{\omega}_r = \omega_r - \hat{\omega}_r$ and $\tilde{\theta} = \theta - \hat{\theta}$. The *error dynamics* can, using (3.7)–(3.11), now be expressed as

$$\dot{\tilde{\omega}}_r = \dot{\omega}_r - \dot{\hat{\omega}}_r = \dot{\omega}_r - \rho^2 \frac{\omega_r \sin \tilde{\theta}}{\hat{\omega}_r} = \dot{\omega}_r - \rho^2 \frac{\omega_r \sin \tilde{\theta}}{\omega_r - \tilde{\omega}_r} \approx \dot{\omega}_r - \rho^2 \tilde{\theta}, \quad (3.12)$$

$$\dot{\tilde{\theta}} = \dot{\theta} - \dot{\hat{\theta}} = \omega_r - \hat{\omega}_r - 2\rho \frac{\omega_r \sin \tilde{\theta}}{\omega_r - \tilde{\omega}_r} = \tilde{\omega}_r - 2\rho \frac{\omega_r \sin \tilde{\theta}}{\omega_r - \tilde{\omega}_r} \approx \tilde{\omega}_r - 2\rho \tilde{\theta}, \quad (3.13)$$

where the approximations in (3.12) and (3.13) are valid if only small estimation errors are considered, i.e., $\hat{\omega}_r \approx \omega_r$ and $\sin \tilde{\theta} \approx \tilde{\theta}$.

The error dynamics are dependent on the mechanical dynamics through $\hat{\omega}_r$, which, in turn, is governed by the speed controller, or if the PMSM is torque (current) controlled, governed by the open-loop mechanical time constant and load-torque characteristics. Adopting the speed controller reviewed in Section 2.4.2 but replacing the true rotor speed with its estimate, the torque *reference* can, from (2.34), be expressed as

$$\begin{aligned} T_e^{\text{ref}} &= k_p (\omega_r^{\text{ref}} - \hat{\omega}_r) + k_i I_s - b_a \hat{\omega}_r \\ &= k_p [\omega_r^{\text{ref}} - (\omega_r - \tilde{\omega}_r)] + k_i I_s - b_a (\omega_r - \tilde{\omega}_r). \end{aligned} \quad (3.14)$$

Since a nonsalient PMSM is considered in this analysis, the current references are selected as $i_{\hat{d}}^{\text{ref}} = 0$ and $i_{\hat{q}}^{\text{ref}} = 2T_e^{\text{ref}} / (3n_p \hat{\psi}_m)$. The *true* electrical torque T_e is, from (2.26), found as

$$T_e = \frac{3n_p \psi_m i_q}{2} = \frac{3n_p \psi_m}{2} (i_{\hat{q}} \cos \tilde{\theta} - i_{\hat{d}} \sin \tilde{\theta}) \approx \frac{3n_p \psi_m}{2} i_{\hat{q}} \approx T_e^{\text{ref}}, \quad (3.15)$$

where the current dynamics have been neglected, i.e., $i_{\hat{d}} = i_{\hat{d}}^{\text{ref}} = 0$ and $i_{\hat{q}} = i_{\hat{q}}^{\text{ref}}$, and a small position-estimation error is assumed. The closed-loop speed control can now, similar to (2.36) and (2.37), be expressed as

$$\begin{aligned} J\dot{\omega}_r &= n_p (T_e - T_l) - b_{\text{fric}} \omega_r \\ &= n_p (k_p [\omega_r^{\text{ref}} - (\omega_r - \tilde{\omega}_r)] + k_i I_s - b_a (\omega_r - \tilde{\omega}_r) - T_l) - b_{\text{fric}} \omega_r, \end{aligned} \quad (3.16)$$

$$\dot{I}_s = \omega_r^{\text{ref}} - \hat{\omega}_r = \omega_r^{\text{ref}} - (\omega_r - \tilde{\omega}_r). \quad (3.17)$$

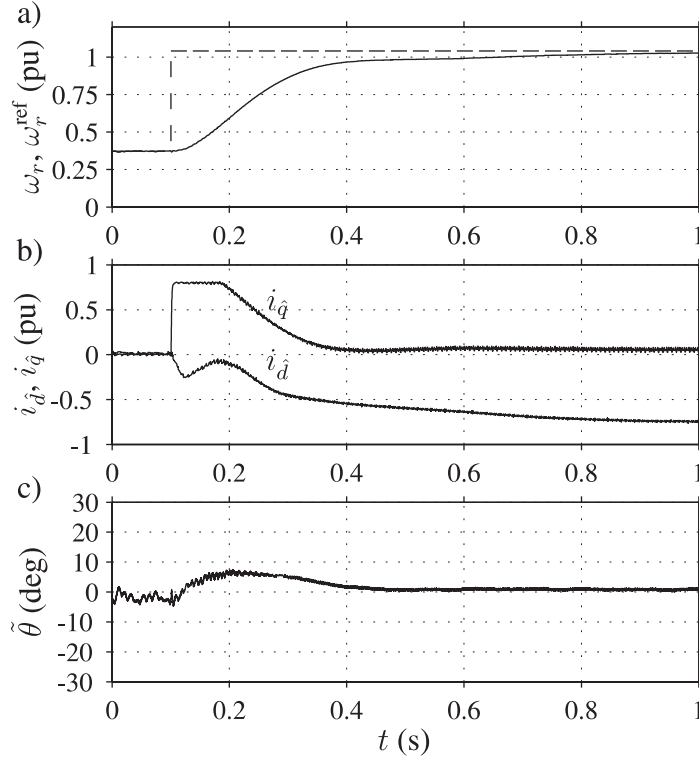


Fig. 3.3 Experimental speed step response using PMSM2 and the PLL-type speed and position estimator [Paper VI].

Eqs. (3.12)–(3.13) and (3.16)–(3.17) now form a fourth-order, linear² system. By defining the state-space vector as $\mathbf{x} = [\omega_r \ \tilde{\omega}_r \ \tilde{\theta} \ I_s]^T$, the input as $\mathbf{u} = [\omega_r^{\text{ref}}]$, and disturbance as $\boldsymbol{\nu} = [T_l]$, respectively, the system can be expressed as

$$\dot{\mathbf{x}} = \mathbf{A}\mathbf{x} + \mathbf{B}\mathbf{u} + \mathbf{E}\boldsymbol{\nu}, \quad (3.18)$$

where the matrices \mathbf{A} and \mathbf{B} are found as

$$\mathbf{A} = \begin{bmatrix} -2\alpha_s & 2\alpha_s & 0 & \alpha_s^2 \\ -2\alpha_s & 2\alpha_s & -\rho^2 & \alpha_s^2 \\ 0 & 1 & -2\rho & 0 \\ -1 & 1 & 0 & 0 \end{bmatrix}, \quad \mathbf{B} = \begin{bmatrix} \alpha_s \\ \alpha_s \\ 0 \\ 1 \end{bmatrix}, \quad \mathbf{E} = \begin{bmatrix} -n_p/J \\ -n_p/J \\ 0 \\ 0 \end{bmatrix}, \quad (3.19)$$

and $b_{\text{fric}} \approx 0$ has been assumed. In operator form, (3.18) can be expressed as

$$\mathbf{x}(p) = \underbrace{(p\mathbf{I} - \mathbf{A})^{-1} \mathbf{B}}_{\mathbf{G}(p)} \mathbf{u}(p) + \underbrace{(p\mathbf{I} - \mathbf{A})^{-1} \mathbf{E}}_{\mathbf{S}(p)} \boldsymbol{\nu}(p). \quad (3.20)$$

²The system is linear due to the approximations made during the derivation process. A more rigorous linearization around the equilibrium point $[\omega_r^* \ \tilde{\omega}_r^* \ \tilde{\theta}^* \ I_s^*]^T = [\omega_r^{\text{ref}} \ 0 \ 0 \ I_s^*]^T$ (the expression for I_s^* is omitted here to save space) yields the same result.

3.2. Some Properties of a PLL-Type Estimator

From (3.20), the following relation is obtained

$$\omega_r(s) = \underbrace{\mathbf{G}_{1,1}(p)}_{G_{cl}(p)} \omega_r^{\text{ref}}(p) + \underbrace{\mathbf{G}_{1,2}(p)}_{S(p)} T_l(p). \quad (3.21)$$

The expressions for the closed-loop dynamics $G_{cl}(p)$ and the sensitivity to the load-torque disturbance $S(p)$ are now found as

$$G_{cl}(p) = \frac{\alpha_s(p + \alpha_s)(p + \rho)^2}{p^2(p + \rho^2)^2 + 2\alpha_s\rho^2p + \alpha_s^2\rho^2}, \quad (3.22)$$

$$S(p) = -\frac{n_p p(p + \rho)^2}{J(p^2(p + \rho^2)^2 + 2\alpha_s\rho^2p + \alpha_s^2\rho^2)}. \quad (3.23)$$

The closed-loop dynamics and sensitivity for the speed controller when assuming that the true rotor position is *known* were derived in (2.41). Comparing (3.22) and (3.23) with (2.41), it is apparent that the closed-loop dynamics, as well as the sensitivity to the load-torque disturbance, have changed. The poles of the closed-loop dynamics are governed by the roots of the denominator in $G_{cl}(p)$. Using the Routh-Hurwitz stability criterion, it is found that $\alpha_s < \rho/2$ is a necessary condition for stability.

To avoid dependence on the number of pole pairs and inertia, $S'(p)$ is introduced as $S'(p) = JS(p)/n_p$. Fig 3.4 shows how $|S'(j\omega)|$ varies as α_s is increased. In order to avoid confusion due to the different units, the per-unit system is *not* adopted in Fig 3.4 and $\rho = 110$ rad/s is assumed. As seen in the figure, if the desired bandwidth of the speed controller is considerably lower than the estimator dynamics, i.e., $\alpha_s \ll \rho$, the sensitivity to the load-torque disturbance $|S'(j\omega)|$ is similar both in the case when the rotor position is estimated (solid lines) and when it is known (dashed lines). However, as α_s increases, the sensitivity increases dramatically for higher frequencies if the rotor position is estimated. Hence, reduced performance can be expected.

At low speeds, the estimator gains are chosen differently to avoid excessive gains, i.e., from (3.10) and (3.11),

$$\gamma_1 = \frac{\hat{\omega}_r \rho^2}{\omega_\Delta \hat{\psi}_m}, \quad \gamma_2 = \frac{2\rho \text{sign}(\hat{\omega}_r)}{\omega_\Delta \hat{\psi}_m}, \quad (3.24)$$

where ω_Δ is the speed limit below which this gain setting should be used (i.e., 0.1–0.2 pu). Performing the same analysis as above (assuming $\hat{\omega}_r > 0$; a similar analysis, resulting in identical expressions, can be made also for $\hat{\omega}_r < 0$) results in the following expression for the sensitivity function

$$S(p) = -\frac{n_p p(\omega_\Delta p + \omega_r^{\text{ref}} \rho)^2}{J(\omega_\Delta^2 p^4 + 2\rho\omega_\Delta \omega_r^{\text{ref}} p^3 + (\omega_r^{\text{ref}})^2 \rho^2 p^2 + 2\alpha_s \rho^2 (\omega_r^{\text{ref}})^2 p + \alpha_s^2 \rho^2 (\omega_r^{\text{ref}})^2)}. \quad (3.25)$$

As seen, the sensitivity is now also dependent on the reference speed ω_r^{ref} . By applying the Routh-Hurwitz stability criterion to the closed-loop system, it is found that $\omega_r^{\text{ref}} >$

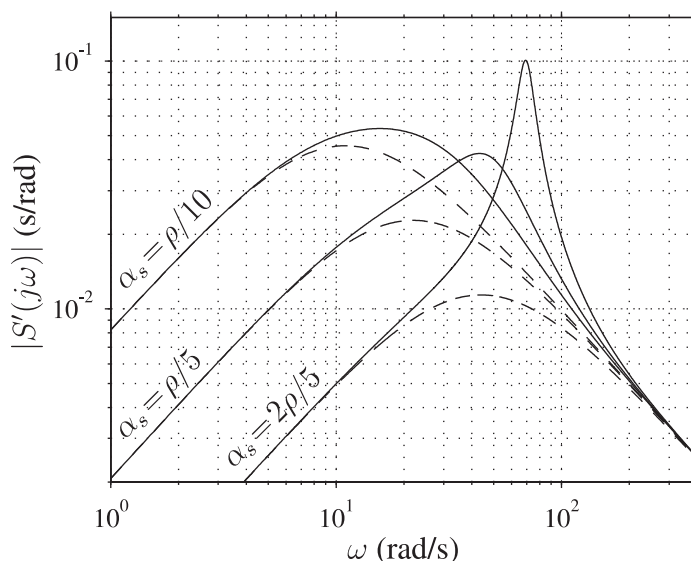


Fig. 3.4 The sensitivity to load-torque disturbances when α_s is varied. Solid lines correspond to when the rotor position is estimated, represented by (3.23). Dashed lines correspond to when the rotor position is known, represented by (2.41).

$(2\alpha_s\omega_\Delta)/\rho$ is a necessary condition for stability. Also here, $S'(p)$ is introduced as $S'(p) = JS(p)/n_p$. Fig. 3.5 shows how $|S'(p)|$ varies as ω_r^{ref} is reduced from $\omega_r^{\text{ref}} = \omega_\Delta$, down to $\omega_r^{\text{ref}} = (2\alpha_s\omega_\Delta)/\rho$, i.e., down to the limit of stability. Also in Fig. 3.5, the per-unit system is *not* adopted and $\rho = 110$ rad/s is assumed. It is clearly seen that the sensitivity to load-torque disturbances drastically increases as the rotor speed approaches the limit of stability.

The analysis presented above illustrates two general problems regarding speed and position estimation.

Reduced Obtainable Mechanical Bandwidth: Fig. 3.4 shows that the dynamics of the speed controller and estimator become coupled when the desired bandwidth of the speed controller (α_s) is increased. Recall also that the PLL-type estimator was derived with the assumption that the closed-loop current dynamics could be neglected, i.e., $\rho \ll \alpha_c$ should be fulfilled. Hence, adopting the speed and position estimator puts an upper limit on the bandwidth of the mechanical dynamics, i.e., $\alpha_s \ll \rho \ll \alpha_c$ must be fulfilled for a proper, decoupled operation of the speed-, estimator-, and current-control loops. If the rotor position is known, only $\alpha_s \ll \alpha_c$ must be fulfilled which allows for a faster speed-control loop. When signal-injection based methods are used for the estimation of speed and position, an error signal of the form $e = K_e \sin 2\tilde{\theta}$ is used to update the speed and position estimates. The factor K_e is a known constant which depends both on the amplitude and frequency of the injected carrier signal as well as the amount of rotor saliency. Performing an analysis similar to the one above results in expressions for the closed-loop dy-

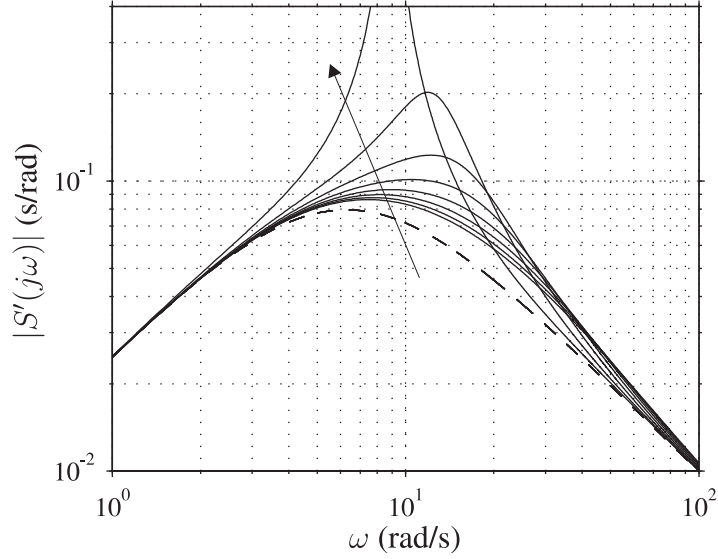


Fig. 3.5 The sensitivity to load-torque disturbances as ω_r^{ref} is reduced from $\omega_r^{\text{ref}} = \omega_\Delta$ down to $\omega_r^{\text{ref}} = (2\alpha_s\omega_\Delta)/\rho$. The arrow represents the direction of *decreasing* ω_r^{ref} . The dashed line corresponds to when the rotor position is known.

namics and sensitivity identical to (3.22) and (3.23), i.e., this method of estimation also puts an upper limit on the obtainable bandwidth of the mechanical dynamics. However, it should be emphasized that this upper limit is not critical for a wide range of applications which the following numerical example demonstrates. Assume that the bandwidth of the closed-loop current control is selected to obtain a 10%–90% rise time of 1 ms. Hence, $\alpha_c = \ln 9/1 \cdot 10^{-3} \approx 2200$ rad/s. In order to obtain $\alpha_s \ll \rho \ll \alpha_c$, ρ and α_s are separated by a decade, i.e., $\rho = \alpha_c/10$ and $\alpha_s = \rho/10 = 2200/100 = 22$ rad/s = 3.5 Hz. Although a mechanical bandwidth of 3.5 Hz is enough for several applications, it can be further increased by reducing the separation between the three control loops, e.g., by choosing $\rho = \alpha_c/5$ and $\alpha_s = \rho/5 = 88$ rad/s which corresponds to 14 Hz, essentially excluding only certain servo applications. A systematic tuning of the specific drive may improve the obtainable mechanical dynamics even further.

Worsened Stability Properties at Low Speeds: The nature of the second problem is illustrated in Fig. 3.5; the sensitivity to load-torque disturbances increases rapidly as speed decreases. This is due to the fact that the gains γ_1 and γ_2 cannot continue to increase as the speed decreases since this would lead to a high sensitivity to noise and parameter errors which, in practice, are always present (an analysis of this phenomenon is presented in [62]). Of course, if signal-injection based estimation is used, the amplitude of the error signal (K_e) is independent of ω_r . Hence, in this case the gains (γ_1 and γ_2) do not have to change as the rotor speed varies and stability can be maintained for all speeds.

3.2.3 Global Stability

The analysis presented above was carried out by linearizing the error dynamics and adopting methods from classical control theory. The approximations made during the linearization process can very often be justified; only small estimation errors in speed and position can be allowed during operation. However, there exist situations when initial, large estimation errors are very difficult to avoid. Such situations include an initiation of the estimator when the rotor is rotating at an unknown speed and also low-speed operation of nonsalient PMSMs when back-EMF based methods are relied on (see further Section 3.3.2). For such situations, the local stability properties, obtained by linearizing the system around a specific equilibrium point, are not sufficient and *global* stability properties must be examined.

The error dynamics of the PLL-type estimator are governed by (3.12) and (3.13). For a constant ω_r , $\dot{\omega}_r = 0$ can be assumed³. Since the system is of second order, drawing phase portraits is a useful technique for analyzing the system's behavior far away from the equilibrium points and by doing this, an interesting property is revealed.

Fig. 3.6 shows a phase portrait of (3.12) and (3.13) where $\hat{\omega}_r \approx \omega_r$ has been assumed. Of particular importance are the *separatrices*, i.e., the solutions that converge to the saddle points at $\tilde{\omega}_r = 0$, $\tilde{\theta} = n\pi$, n odd. These divide the phase plane into convergence regions. If the estimator is initialized in the region enclosed by separatrices A and B, $\tilde{\theta}$ will converge to 0. However, if initialized in the region enclosed by separatrices B and C, $\tilde{\theta}$ will converge to 2π , and so forth. This means that the estimator falls one or more revolutions behind the machine (*cycle slips* in PLL terminology [71] and *pole slipping* in synchronous machine terminology [61]); synchronism is temporarily lost. Note that the separatrices are stacked densely for $|\tilde{\omega}_r| > 3\rho$; initialization at $\tilde{\theta} \approx 0$, $|\tilde{\omega}_r| > 3\rho$ may, thus, lead to numerous cycle slips, giving a long re-synchronization process. This is unacceptable, and should, if possible, be avoided.

While selecting a larger ρ would improve the situation, this also increases the estimator's sensitivity to disturbances, as discussed above. Therefore, ρ should only be selected large enough to cope with accelerations that occur normally, while a function by which abnormally rapid accelerations can be handled safely should be incorporated. A method to achieve this, as well as a more detailed analysis of the global stability properties of the improved estimator, is presented in [Paper I].

3.2.4 Impact of Rotor Saliency

A salient PMSM offers the possibility to adopt signal-injection based estimation methods in order to obtain proper speed and position estimates at very low, including zero, speeds. Although this is an obvious advantage, the high-frequency carrier signal added causes,

³This can in practice be relaxed to a so-called quasi-constant ω_r ; the estimator is assumed to converge much faster than the speed varies.

3.2. Some Properties of a PLL-Type Estimator

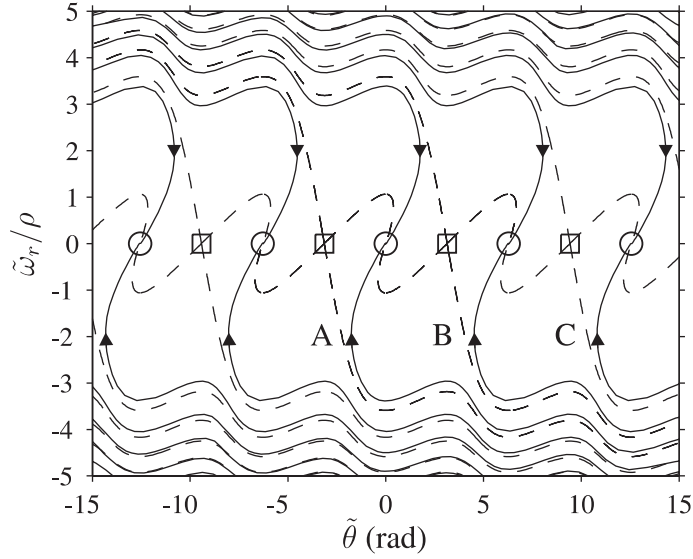


Fig. 3.6 Phase portrait of the error dynamics of the PLL-type estimator. Solid lines indicate solution curves. The dashed lines are separatrices of the saddle points at $\{\tilde{\omega}_r, \tilde{\theta}\} = \{0, n\pi\}$, n odd, indicated by squares. The circles mark the stable equilibrium points at $\tilde{\theta} = n\pi$, n even.

at least to some extent, additional noise, torque ripple, and losses. Hence, it is desirable to rely on signal-injection based estimation only in the very low speed range and make a transition to a back-EMF based estimation method for higher speeds.

Rotor saliency also affects back-EMF based estimation methods and this should be taken into consideration when designing an algorithm for speed and position estimation. Fig. 3.7 shows simulation results obtained using MATLAB⁴, where the parameters for PMSM⁵ are adopted with the exception of L_d and L_q which are varied in order to demonstrate the impact of different rotor saliencies. The PMSM is operated at the constant speed $\omega = 0.1$ pu and the current references are set to $i_d^{\text{ref}} = 0$, and $i_q^{\text{ref}} = -0.75$ pu. The desired rise time of the closed-loop current controller t_r is selected to $t_r = 1$ ms, hence, the bandwidth of the current controller α_c is found as $\alpha_c = \ln 9/t_r$. The estimator bandwidth ρ is selected as $\rho = \alpha_c/5$. With the intention of demonstrating how the estimator converges from an estimation error, a speed estimation error is introduced at $t = 0.1$ s by subtracting 0.03 pu from $\hat{\omega}_r$. Fig. 3.7 shows that there is a significant difference in how the estimator converges depending on the amount of rotor saliency. For the case when $L_d = 0.4L_q$ and $L_q = 0.9$ mH, damping is worsened, causing a significant oscillation in both the estimated speed and position (choosing $L_d = L_q = 0.4 \cdot 0.9$ mH = 0.36 mH produces results similar to $L_d = L_q = 0.9$ mH).

Although the simulation results presented in Fig. 3.7 might appear as a somewhat academic exercise (the operating point and choice of parameters were carefully selected),

⁴MATLAB is a registered trademark of The Mathworks, Inc., Natick, Massachusetts, U.S.A.

⁵More details concerning the PMSM can be found in Appendix B.

they demonstrate that certain operating points can exist where the damping of the estimator is reduced, thus leading to a worsened quality of the speed and position estimates, and that this reduced damping is “caused” by rotor saliency. An analysis of this phenomenon is presented in [Paper II] and further developed in [Paper III] where design guidelines for the PLL-type estimator are derived in order to maintain proper damping (and a sufficiently small position estimation error) for all rotor speeds.

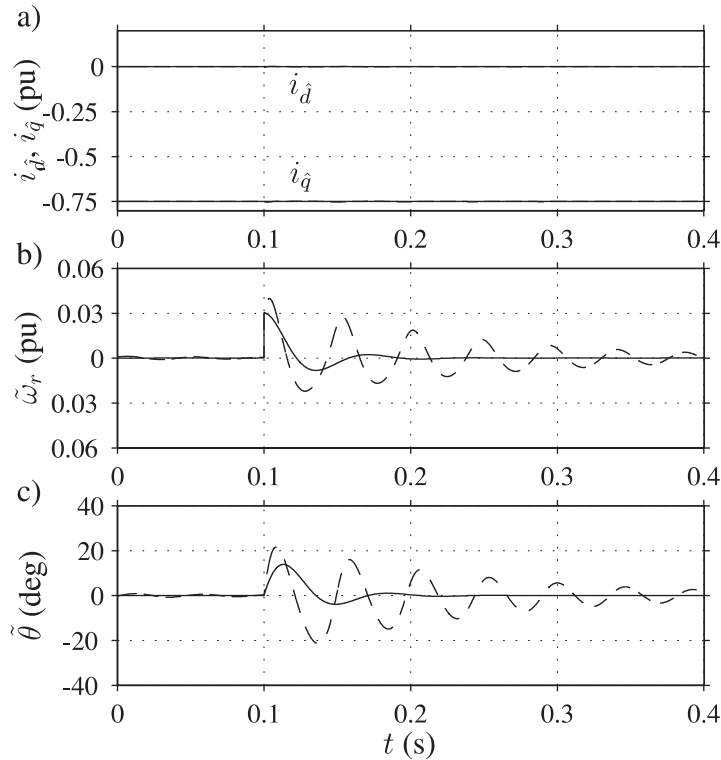


Fig. 3.7 Convergence procedure of the PLL-type estimator when rotor saliency is varied. Parameters corresponding to PMSM1 with the exceptions $L_d = L_q = 0.9$ mH (solid lines) and $L_d = 0.4L_q$, $L_q = 0.9$ mH (dashed lines).

3.3 Recent Developments

3.3.1 Signal-Injection Based Estimation

Sensorless control above the low-speed range is today not a major research challenge and several algorithms have been proposed and implemented in commercial drives. Also low-speed operation, including zero speed, using signal-injection based estimation techniques has been implemented in commercial drives adopting salient PMSMs.

However, sensorless control in the low-speed region for nonsalient PMSMs is still an active area of research. As mentioned previously, the term nonsalient is somewhat

misleading since even PMSMs using surface-mounted magnets possess a small saliency which is induced by saturation effects. Several different approaches have been proposed in order to utilize this induced saturation together with some kind of signal-injection based estimation technique.

Due to the low level of effective saliency, the signal-to-noise ratio can be very small and additional non-ideal effects, such as the inverter dead time [49] and inductance cross saturation [25], [30], [8], must often be compensated for to obtain proper estimates of speed and position. For matrix converters, the non-ideal effects due to the converter itself can be much smaller when compared to standard voltage source inverters. Therefore, a better quality of the speed and position estimates can be obtained when signal-injection based estimation is applied to surface-mounted PMSMs [3]. In [70], signal-injection based estimation is implemented using a surface-mounted PMSM and the relative shift in stator flux during load is compensated for using a commissioning process during which the rotor position is measured. In [42], the low signal-to-noise ratio when implementing signal-injection based estimation is tackled by injecting a very large amplitude of the carrier signal; corresponding to an amplitude of 100 V, which can be considered very high since the rated voltage of the particular PMSM is 180 V.

It is a well known fact that signal-injection based estimation methods cannot determine the correct polarity of the rotor. An additional startup procedure is therefore needed in order to determine the correct polarity. In [31], the correct polarity is determined on a surface-mounted PMSM by injecting a very large current amplitude (approx. 150% of rated current) during a short initiation process.

3.3.2 Back-EMF Based Estimation at Low Speeds

From the discussion and references presented above, it is evident that accurate speed and position estimates in the low-speed range when using nonsalient PMSMs is not straightforward. The problems associated with the low signal-to-noise ratio is circumvented by using very large amplitudes of the injected carrier signal, different converter topologies (i.e., the matrix converter), and often a careful tuning procedure is needed in order for the drive to operate properly.

Obviously, signal-injection based estimation techniques are attractive for a wide range of applications. However, several applications exist where nonsalient PMSMs are adopted and high performance in the low-speed region is not critical as long as startup, and possibly also rotation reversals, can be guaranteed, preferably also under load⁶. Naturally, it is important that the estimator has a low sensitivity to parameter variations and a simple implementation procedure is vital in order to allow an easy implementation of the

⁶From the analysis presented in Section 3.2, it is apparent that the PLL-type estimator, when relying on back-EMF based estimation, cannot fulfill such a goal since the estimator was proved to be unstable below a certain speed.

estimator in different PMSM drives.

Back-EMF-based estimators that give reliable start and rotation reversal under load are relatively rare. In [57], it is shown that, for the algorithm in [53], stable startup from any initial rotor position is not guaranteed, but can be, if the algorithm is modified. In [9], a countermeasure against rotation in the wrong direction is added to an extended-Kalman-filter-type algorithm in order to achieve a reliable start. The algorithm in [78] is experimentally shown to give guaranteed synchronization, although no strict proof thereof is presented.

An alternative back-EMF based estimator is presented in [Paper IV] that is based on the well known “voltage model.” A flowchart of the proposed estimator is shown in Fig. 3.8. Since the back EMF vanishes as the rotor speed becomes zero, stable operation at zero speed cannot be guaranteed for any back-EMF based method. Therefore, it is vital that the estimator has good *global* stability properties in order to converge to correct speed and position estimates from any initial condition. In [Paper IV], it is shown that the proposed estimator has suitable global stability properties, and that the estimator’s sensitivity to stator resistance mismatch can be avoided by manipulating the current in the \hat{d} direction. Fig. 3.9 shows simulated startups using the estimator presented in [Paper IV]. The initial values of the (unknown) rotor position are varied and the PMSM is connected to a load with fan characteristics, i.e., the load torque T_l is proportional to the square of the true rotor speed ($T_l = 0.5$ pu when $\omega_r = 0.1$ pu). The parameters of the PMSM correspond to PMSM2⁷ and reasonable parameter errors are introduced into the simulation. As seen, a proper startup is achieved for all initial rotor positions. Experimental results are presented in the paper⁸ and the appended piece of C-code clearly demonstrates how easily the estimator can be implemented.

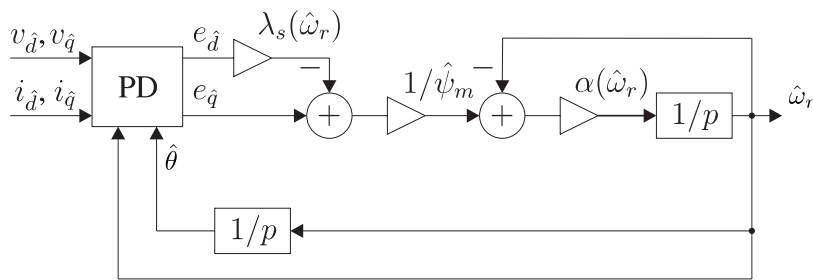


Fig. 3.8 Flowchart of the estimator presented in [Paper IV]. Design guidelines for the parameters $\alpha(\hat{\omega}_r)$ and $\lambda_s(\hat{\omega}_r)$ are presented in the paper.

⁷More details concerning the PMSM can be found in Appendix B.

⁸The experimental results were obtained by Jansson and Leksell, the first and fourth authors of [Paper IV].

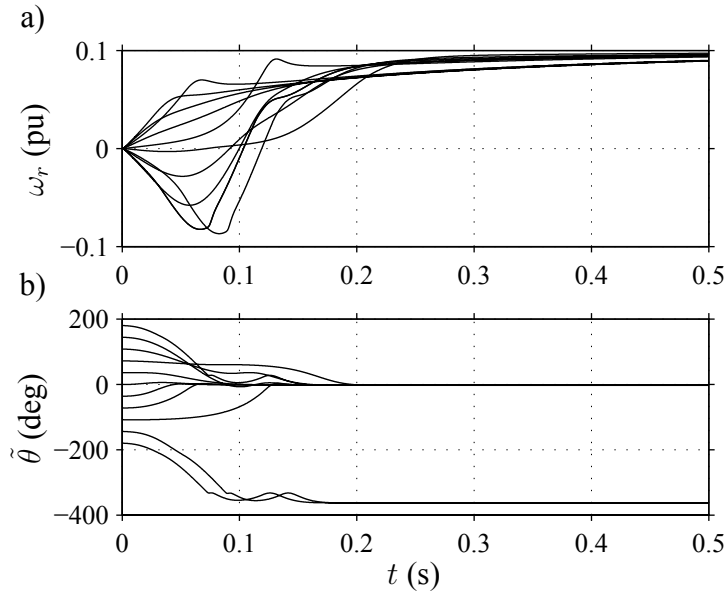


Fig. 3.9 Simulated startups from different (unknown) rotor positions for a PMSM connected to a quadratic load using the estimator presented in [Paper IV]. The inertia J is set to $J = 1 \text{ kgm}^2$ and the machine parameters correspond to PMSM2. Current control: 2 ms of desired current rise time. Estimator parameter (see [Paper IV]): $\lambda = 2$. Parameter errors: $\hat{L}_d = 0.8L_d$, $\hat{L}_q = 0.8L_q$, $\hat{R}_s = 0.5R_s$.

3.3.3 Outlook

The rapid development of different PMSM designs that has been underway during the past two to three decades clearly highlights the advantages, in terms of increased torque-to-inertia ratio, power density, and efficiency, that can be obtained by adopting permanent magnets in electric machines. The fact that the rotor position must be known for proper operation has, to a large extent, been circumvented by the development of different types of estimators which have successfully been implemented in a wide range of PMSM drives. This has also been facilitated by the fact that PMSMs with interior-mounted magnets, where the level of rotor saliency and magnet flux can be easily tailored depending on the application, often possess a significant saliency. Therefore, signal-injection based estimation in the zero- and low-speed range can often be implemented with ease, and accurate estimates of speed and position can be obtained in the whole speed range.

It can be expected that guidelines, used during the design stage of the machine, will be further developed in order to guarantee that accurate, signal-injection based, speed and position estimates are guaranteed in conjunction with low losses, noise, and torque ripple due to the additional carrier signal added (recent references concerning this emerging topic include [8] and [39]). It is likely that the automotive industry will act as an important driving factor here since the cost reduction associated with the removal of the rotor position sensor, together with the above mentioned advantages with PMSMs, make such

Chapter 3. Speed and Position Estimation

drive solutions very attractive in automotive applications.

For nonsalient PMSMs, an interesting topic of further research is to compare the low-speed performance of the different types of back-EMF based estimators that have been proposed in the literature; preferably implemented in several different experimental setups. Such a comparison should include aspects such as ease of implementation, quality of speed and position estimates during transients, and sensitivity to parameter variations as well as non-ideal effects due to the inverter.

Combining speed and position estimation with on-line estimation of machine parameters can improve performance as demonstrated in [38]. An interesting approach that may be fruitful is to investigate if the recursive-least-square based method of parameter estimation presented in [38] can be merged with the estimator presented in [Paper IV] in order to further improve low-speed performance.

In applications where drive failure cannot be tolerated, adopting a speed and position estimator in the event the function of the position sensor fails improves reliability of the system [29], [43]. Hence, it can be expected that techniques for correctly detecting a faulted position sensor, as well as a commissioning process in order to rapidly obtain correct speed and position estimates, will be further developed and adopted in various automotive applications.

3.4 Summary of Chapter

This chapter focused on the problem of speed and position estimation of PMSM drives. An introduction outlining two different categories of methods to obtain speed and position estimates was presented. Two general problems demonstrating the limitation put on mechanical bandwidth and reduced performance at low speeds were presented as a result of analyzing a PLL-type speed and position estimator for which several improvements and additions are presented in the included papers of this thesis. Finally, possible opportunities for further research were outlined.

Chapter 4

On Fault Tolerance and Fault Characteristics of PMSM Drives

This chapter focuses on the impact of electrical faults for PMSM drives in various automotive applications. Means to provide fault tolerance to inverter faults are discussed in particular. The impact of electrical faults on a propulsion application is also investigated which provides a background for the case studies presented in [Paper VII] and [Paper VIII].

4.1 Introduction

As discussed in Chapter 1, electric drives adopting permanent-magnet machines, both with sinusoidal (PMSM) and trapezoidal (BLDC) excitation, are suitable for a wide range of applications in EVs and HEVs. These applications include not only propulsion but also steer- and brake-by-wire systems, active suspension, and other electrical subsystems. Naturally, proper operation of functions such as steer- and brake-by-wire are of utmost importance and their failure cannot be tolerated since this would drastically compromise passenger safety. Despite that the automotive industry is very cost sensitive, there are strong incentives to increase system costs in order to improve the level of fault tolerance when mechanical actuators are being replaced by their electrical counterparts for certain, fault critical, applications in the vehicle. For PMSM drives used for propulsion, however, it is evident that increasing the level of reliability, which is often afflicted with a significant cost increase, typically cannot be motivated if a fault is not likely to significantly increase the accident risk or if a post-fault capacity (i.e., “limp home”) cannot be economically motivated for the specific vehicle model.

This chapter focuses on fault responses of PMSM drives as well as methods for increasing the level of fault tolerance for such drives in automotive applications. The term *drive*, as it is used in this thesis, pertains to both the electric machine as well as its corresponding inverter. Although faults can arise in other parts, e.g. bearings and gears,

such types of faults are omitted here; only a distinction between faults originating in the machine and faults originating in the inverter is made. After a brief introduction to the main types of electrical faults that can afflict a PMSM drive, the behavior of PMSM drives to a specific class of faults (inverter faults) are treated in more detail along with an outline of the contributions presented in [Paper VI].

The impact of electrical faults for PMSM drives used for propulsion are investigated in [Paper VII] and [Paper VIII] and supplementary details concerning these investigations complete this chapter. The specific vehicle considered in both of these papers is equipped with four in-wheel motors which can be controlled independently. This type of vehicle provides an “in-built” fault tolerance since if one, or several, of the in-wheel motors fails, it is possible to handle the fault by controlling the remaining, still functioning, in-wheel motors and bring the vehicle safely to rest or continue driving with only minor deviations in the intended driving trajectory.

4.2 Fault-Tolerant Machines

Different types of short-circuits, such as an inter-turn short circuit or a winding-to-frame short circuit, are particularly problematic for electric machines equipped with permanent magnets in the rotor since this excitation cannot easily be removed and continues to excite the stator winding as long as the rotor rotates. Hence, a rapid detection of such a fault is needed in order to avoid any further insulation breakdown caused by the large current that builds up in the shorted turn in order to counteract the machine excitation.

The seriousness of electrical faults arising in permanent-magnet machines has led to the development of fault-tolerant machines whose designs differ rather significantly from conventional machines. Fault tolerance is achieved by electrically, thermally, and magnetically isolating each phase from the other phases. Mutual coupling between phases is avoided by having only one phase winding on each slot and mechanical and thermal isolation can be accomplished by placing the windings around every other tooth (see, e.g., Figs. 1–3 in [55]). In order to reduce the overrating of each phase, more than three phases are used (often four to six phases) which, to further increase the level of fault tolerance, are fed by separate H-bridge inverters. If a shorted turn or an inverter-switch short circuit is detected, the fault is handled simply by shorting the faulted phase using the H-bridge inverter. In order to avoid too high currents when the phase is shorted, the machine can be designed with a per-unit inductance equal to the back EMF which effectively limits the short-circuit current to its rated value [6], [55].

Several of the design goals that need to be fulfilled in order to achieve fault tolerance are contradictory when compared to conventional machine designs. The drawbacks associated with the achieved fault tolerance include an increase in weight, reduced efficiency, and increased total cost. If future demands for fault-tolerant machines arise for propulsion applications, this may favor other machine types such as induction and switched-

reluctance machines. However, it appears as though fault-tolerant permanent-magnet machines can be competitive in certain niche applications such as fuel pumps and actuators for aircraft applications [4], [54].

To conclude, it is apparent that the difficulty in removing the excitation from the permanent magnets is a significant drawback associated with permanent-magnet machines and the author of the present thesis is doubtful whether these types of fault-tolerant machines will become common in automotive applications.

4.3 Inverter Reliability

In vehicle propulsion applications, the power flow through the inverter is essentially defined by the driving cycle of the vehicle. The power demand throughout a driving cycle can vary extensively due to starts, stops, accelerations, and braking of the vehicle. Due to these large variations in power demand, the inverter switches have to endure large temperature variations (thermal cycles). For *insulated gate bipolar transistors* (IGBTs), the mismatch between the thermal expansion coefficients of the aluminum wire and the silicon chip is the cause of shear stresses on the bonding interfaces which can lead to wire bond breaking [58], [64]. In order to predict the lifetime of an IGBT, the number of thermal cycles that the IGBT endures during operation must be correctly determined. This is not trivial and different methods are presented in [18] and [36]. Apart from the inverter switches, the dc-link capacitor is an important part of the inverter and should be taken into account when estimating the reliability of the inverter. The results in [36], however, indicate that the methods for estimating inverter reliability of drives used in propulsion applications have, because of the significant variations in power flow due to the driving cycle, not fully matured and do not (yet) provide results with sufficient accuracy.

In order to improve inverter reliability, the IGBTs (and corresponding diodes) can be merged together with the gate drives and additional control circuitry into a single power module. Such power modules are often referred to as *intelligent power modules* (IPMs). The additional control circuitry can provide protection functions, by gating off the IGBTs, such as over-temperature protection, short-circuit protection, and protection from under-voltage from the supply to the internal gate drives and control circuitry [37], [40], [59].

4.3.1 Response of PMSMs to Inverter Faults

It is apparent that reliability prediction of inverters in propulsion applications is still an area of active research. Furthermore, the level of fault tolerance is highly dependent on the specific application in the vehicle. Another important factor that determines whether or not means for achieving fault tolerance are needed is how the PMSM responds to different types of inverter faults. Since the excitation due to the permanent magnets cannot be removed, the behavior of PMSMs during inverter faults, and not only faults arising

inside the machine, differs significantly when compared to, e.g., induction and switched-reluctance machines.

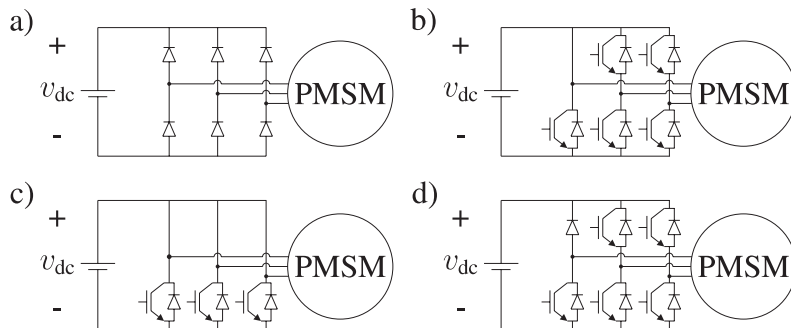


Fig. 4.1 Different types of inverter faults: a) Inverter shutdown; b) Single-phase short circuit; c) Balanced short circuit; d) Single-switch open circuit.

The response of PMSMs to different types of inverter faults has been thoroughly investigated in [41], [56], [75], [76] but key results are illustrated also here for the sake of clarity. The three-phase PMSM model presented in Chapter 2 was implemented in MATLAB together with the reviewed current controller. Parameters corresponding to PMSM2 were used and, in order to simulate inverter faults, the voltages were generated by assuming a constant dc-link voltage and implementing a *pulse-width modulation* (PWM) with a symmetrical, triangular carrier. The switches were assumed ideal, i.e., the forward and resistive voltage drops of the transistors and corresponding diodes were neglected. The different types of inverter faults considered are illustrated in Fig. 4.1 and described below. Apart from the described inverter faults, if both the upper and lower transistor in an inverter leg are gated on simultaneously, the dc link is short circuited. Although this is a very critical situation, it is assumed that the inverter legs are equipped with an in-built short-circuit protection (like in IPMs) that, in the event of over current, rapidly gates off both transistors.

Inverter Shutdown: The fault illustrated in Fig. 4.1a) is referred to as an *inverter shutdown* [41]. Here, the gate signals to the transistor switches, for some reason, vanish. Reasons for the origin of such a fault include; failure of the gate drive (supplying the gate pulses to all of the transistors), a signal-cable breakdown, or loss of power to the control circuitry. Below a certain speed, the induced voltage originating from the permanent magnets is lower than the dc-link voltage. Consequently, no current will flow through the diodes of the inverter and the output torque is zero. At higher speeds, i.e., when field-weakening is applied, the induced voltage can be higher than the dc-link voltage and power is then fed from the PMSM into the dc link. Assuming a constant dc-link voltage, the current is dictated only by machine impedances and voltage drops across the diodes (the latter effect is, as mentioned above, not included in the present simulation).

Fig. 4.2a) shows a simulation illustrating an inverter shutdown when the PMSM is operating deep in field-weakening mode ($i_d = -1.5$, $i_q = 0.5$ pu) at constant speed ($\omega_r = 1.5$ pu). At $t = 5$ ms, the inverter shuts down and power is fed from the PMSM to the dc link (essentially, the sign of i_q changes). The steady-state waveforms of i_d and i_q after the inverter shutdown has occurred are not constant, but fluctuate somewhat. This is due to the fact that the induced voltage is not greater than the dc-link voltage at all time instants and, thereby, no current is fed through the diodes. This effect, however, is less pronounced as the rotor speed, and thereby induced voltage, increases.

Single-Phase Short Circuit: A single-phase short circuit is illustrated in Fig. 4.1b) and corresponding simulation results are shown in Fig. 4.2b). The PMSM is operating at moderate speed and load ($\omega_r = 0.5$, $i_d = 0$, and $i_q = 0.5$ pu) and the upper-left transistor is permanently gated on at $t = 5$ ms. As seen, large current amplitudes arise rapidly. Continuing the simulation results in very high, oscillating torque and current waveforms and it is obvious that this must be considered a very severe fault condition [56], [76]. Due to the large current amplitudes obtained, it is very likely that demagnetization of the rotor magnets and inductance saturation arise; phenomena that are not included in the present simulation.

Balanced Short Circuit: A balanced short circuit is illustrated in Fig. 4.1c). A corresponding simulation, shown in Fig. 4.2c), demonstrates the response which is characterized by, after an initial transient, generating action which is limited only by the machine impedances. This fault condition also results in $i_d < 0$ which, if the machine inductance is not sufficiently large, can risk to demagnetize the rotor magnets. However, as compared to the single-phase short circuit, the balanced short circuit can be considered a much less severe fault condition. A controlled balanced short circuit can be initiated from the inverter by gating on all upper (or lower) transistors and leaving the lower (or upper) transistors gated off.

Single-Switch Open Circuit: Failure of a single transistor switch, referred to as a *single-switch open circuit* is demonstrated in Fig. 4.1d). From the simulation results shown in Fig. 4.2d), it is apparent that this fault condition is the most benign of the above in terms of current and torque amplitudes. However, the fault may be problematic due to the fluctuating torque leading to, e.g., problems during startup.

4.3.2 Fault-Tolerant Inverters

A comprehensive survey of different fault-tolerant inverter topologies that have been presented in the literature can be found in [77], and their applications in automotive applications are described in [6]. These fault-tolerant inverters require no or only modest

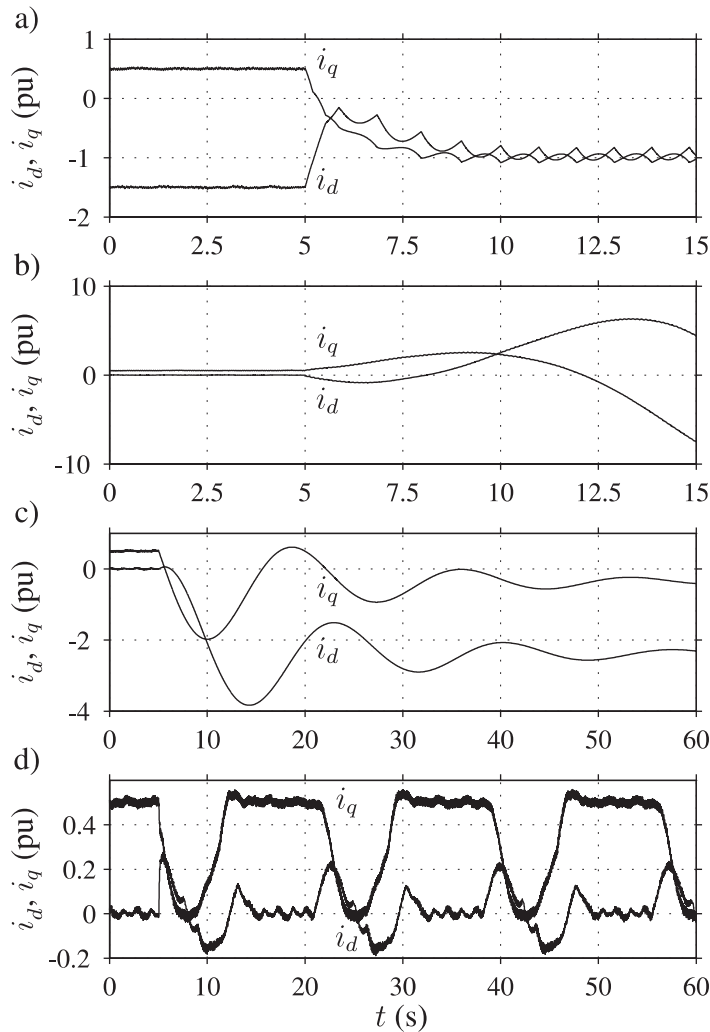


Fig. 4.2 Machine responses during different inverter faults: a) Inverter shutdown; b) Single-phase short circuit; c) Balanced short circuit; d) Single-switch open circuit.

modifications to the corresponding machine, e.g., the requirement that the machine is Y-connected with the neutral point available. From the survey in [77], it is concluded that the cost related to the added fault tolerance is significant and that several of the proposed topologies only provide a reduced amount of output power in fault mode. Consequently, the inverter and machine need to be overrated in order to achieve nominal output power in fault mode. The main reasons for the significant cost increase are the addition of extra inverter legs and the fact that there must be means added to interrupt the current in the faulted phase. This requires isolation devices connected in series with each phase of the machine. Such a device can be realized using back-to-back connected thyristors connected in series with each phase that, in pre-fault (normal) mode, are continuously gated on. The faulted phase can then be isolated by gating off both of the thyristors which extinguishes the current at the next zero crossing. Naturally, these types of isolation devices

will, apart from adding cost to the system, also add on-state losses which results in a reduction in efficiency also in pre-fault mode, i.e., before a fault has occurred. Although phase isolation can also be achieved using fuses, such a solution is problematic since these devices are uncontrollable, i.e., cannot deliberately be turned off by the control system. In [56] and [76], it is shown that a controlled balanced short circuit is a suitable mean to reduce the severity of several of the faults described above provided that the machine inductance is sufficiently high to limit the short-circuit current within a tolerated range. If such a fault-handling strategy is adopted and the rotation of the PMSM can be interrupted, it may be suitable to use simpler disconnecting switches to reconfigure the fault-tolerant inverter while the rotor is at standstill.

4.3.3 Control Algorithms for a Fault-Tolerant Inverter

In [Paper VI], novel control algorithms are presented for a fault-tolerant inverter configuration which was proposed in [10] by Bolognani *et al.* The main features of this inverter configuration are depicted in Fig. 4.3a). As can be seen, fault tolerance is accomplished by adding an extra inverter leg to the configuration of a standard three-phase inverter. The additional inverter leg is connected to the neutral point of the PMSM which therefore requires a Y-connected machine with the neutral point available. When an inverter fault is detected, the faulted phase is isolated by disconnection. Post-fault operation is then commenced by activating the additional fourth inverter leg which is connected to the neutral point of the machine. The additional inverter leg does not require a connection device if it can be assumed that this leg is not likely to fail, motivated by the fact that it is not active in normal mode.

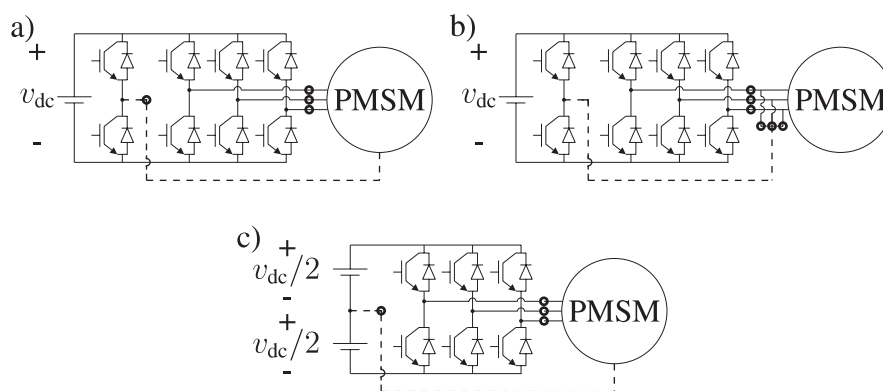


Fig. 4.3 Fault-tolerant inverters (circles indicate additional connection and isolation devices): a) The additional inverter leg connects to the neutral point on the PMSM [10]; b) The additional inverter leg replaces faulted inverter leg directly [63]; c) The neutral point is connected to the midpoint of the dc link [50].

The original configuration proposed in [10] also provides fault tolerance to the situation when both of the transistors in the same inverter leg are gated on. This is ac-

complished by adding fuses in series with each inverter leg. Apart from the reliability problems associated with fuses, this also gives rise to an increased inductance between the transistors and dc-link capacitor and is, consequently, not considered here.

In [63], a fault-tolerant inverter configuration is proposed where the faulted phase is isolated and directly replaced with the additional inverter leg. Such a configuration is shown in Fig. 4.3b). Compared to such a solution, the fault-tolerant inverter shown in Fig. 4.3a) demonstrates, according to the author of the present thesis, the following important differences.

Simpler Connection Device: Since the additional leg, regardless of which phase leg that is faulted, should always be connected to the neutral point instead of to the faulted phase, the connection device can be made simpler. This is particularly beneficial if the inverter is equipped to control several PMSMs using a common dc link and having only one additional inverter leg for redundancy. This inverter leg can then provide fault tolerance to any of the other inverter legs as exemplified in [Paper VI, Fig. 2].

Winding Open-Circuit Faults: In fault mode, the faulted phase is isolated and connected to the other phases only through the neutral point. Consequently, open-circuit faults striking also a phase winding, or its connection to the inverter, can be handled.

Reduced Output Power: The available output power in fault mode is reduced since the current in the remaining phases must increase with a factor of $\sqrt{3}$ and with a factor of 3 in the neutral connection, in order to obtain the same output torque as during normal operation. Typical current waveforms for the inverter in fault mode are shown in Fig. 4.4. As pointed out in [7], if the additional inverter leg is oversized, in terms of current rating, with a factor of $\sqrt{3}$ the available output torque can be increased to a factor $1/\sqrt{3} \approx 0.58$ compared to normal mode.

Saturation Caused by Asymmetrical Supply: Since the machine in fault mode is only fed from two phases, this deliberately introduced asymmetry may cause saturation at different locations inside the machine due to a flux-density distribution with high harmonic content caused by the fact that the stator winding is not perfectly sinusoidally distributed [12].

Modified Control Algorithms in Fault Mode: Since the machine is fed from an asymmetrical supply, the control algorithms need to be modified accordingly. In [Paper VI], novel control algorithms, extending the results in [7], are proposed. These algorithms provide simple modifications to the control algorithms reviewed in Chapter 2 and Chapter 3 in order to obtain closed-loop field-weakening control and speed and position estimation also in fault mode. A method for controlling the neutral-point voltage is also presented so that the available voltage capacity of the inverter

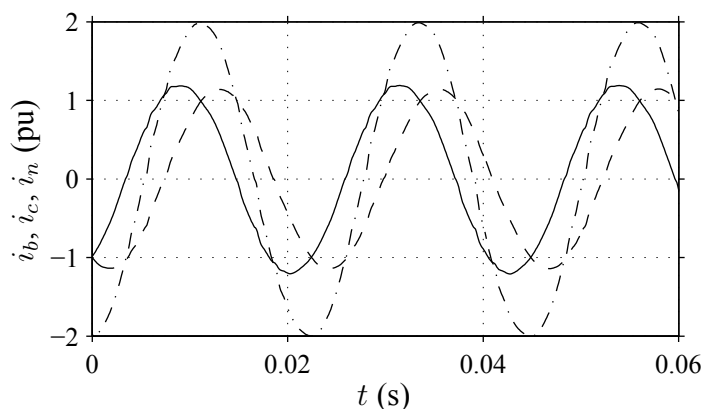


Fig. 4.4 Typical measured current waveforms for the fault-tolerant inverter in fault mode where phase a has been isolated: i_b (solid line), i_c (dashed line), and current in neutral connection (dashed-dotted line).

is the same in both normal and fault modes. Fig. 4.5 shows a MATLAB simulation of a speed step response using the algorithms presented in [Paper VI] and results from a corresponding experiment are shown in Fig. 4.6. The conditions are identical to those presented in Section 3.2.1 with the exception that the inverter is operating in fault mode. Comparing Fig. 4.6 and Fig. 3.3, it is evident that, apart from the small second harmonic arising in $\tilde{\theta}$, $i_{\tilde{d}}$, and $i_{\tilde{q}}$, the results are virtually identical for the two modes of inverter operation.

Remark: The algorithms presented in [Paper VI] can also be applied to the inverter configuration shown in Fig. 4.3c) where the neutral point of the machine is connected to the midpoint of the dc link (this is elaborated on in [Paper IX]). Such a midpoint can be created by connecting capacitors in series. However, the amplitude of the current in the neutral connection is large which must be taken into consideration when choosing the size and type of capacitors. Furthermore, active or passive balancing may also be needed in order for the dc-link voltage to divide evenly between the capacitors.

4.4 Sensor Faults

Apart from faults arising in the machine or inverter, the drive is equipped with different sensors that provide information used by the control system. For a PMSM drive, these sensors typically measure phase currents (at least two of the three phase currents are measured), dc-link voltage (since it is prone to variation if the inverter is fed from a battery source), and rotor position (if it is not estimated). Naturally, if the loss of a sensor means that further operation of the drive is not possible, this class of faults is of equal importance as machine or inverter faults. Fortunately, methods to detect and handle these types of faults have been developed, with automotive applications in mind, both for PMSMs [43]

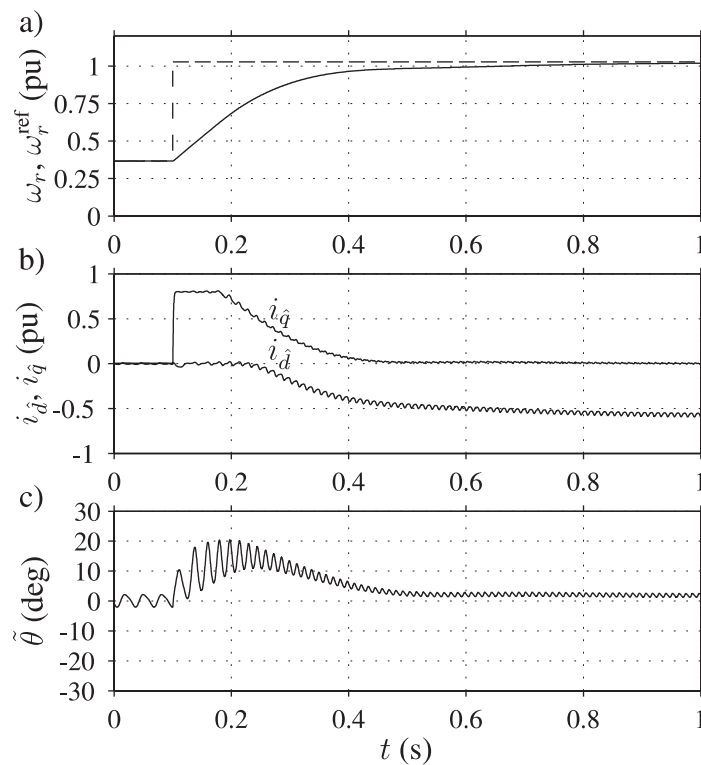


Fig. 4.5 Simulation of a speed step response for the fault-tolerant inverter in fault mode using PMSM2 and the modified PLL-type speed and position estimator.

and induction machines [20]. For each of these sensor faults, methods for detecting the fault are proposed together with modifications of the control schemes in order to continue operation. Similar to fault-tolerant inverters whose control schemes are modified in post-fault mode, the implementation of these schemes can be realized using the high computational capacity of modern DSPs.

4.5 Electrical Faults in a Propulsion Application

As discussed in Section 4.1, the required level of fault tolerance for PMSM drives in automotive applications is dependent on the specific function of the drive. For propulsion applications, the required level of fault tolerance is, apart from the dependency on cost sensitivity, strongly dependent on how the electric drivetrain is constituted. As an example, a fault that causes the electric propulsion to shut down in the parallel-HEV drivetrain shown in Fig. 1.1b) can be less severe than if the same situation arises in the series-HEV shown in Fig. 1.1a). The reason for this is that all propulsion power is not lost in the parallel-HEV since the ICE, due to its mechanical connection to the transmission, may still provide enough power to propel the vehicle.

As the study of the severity of electrical faults in propulsion applications is so

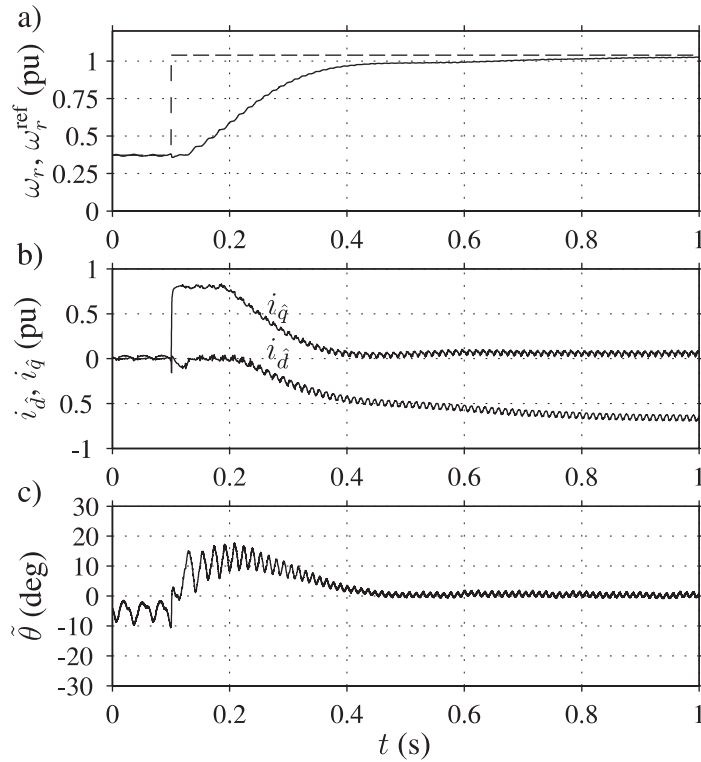


Fig. 4.6 Experimental speed step response for the fault-tolerant inverter in fault mode using PMSM2 and the modified PLL-type speed and position estimator [Paper VI].

strongly dependent on how the electric drivetrain is constituted, the study of this topic is in the present thesis restricted to a case study presented in detail in [Paper VII] and [Paper VIII]. This case study considers an electric vehicle equipped with four in-wheel motors¹. Following the convention used in Fig. 1.1, a flowchart of such a drivetrain is shown in Fig. 4.7. It is assumed that the vehicle is powered from a battery in combination with a supercapacitor² where the latter functions as a buffer that can provide, or absorb, power much more rapidly than the battery whose dynamical response is much slower.

4.5.1 A Vehicle With Individual Control of All Four Wheels

The vehicles in consideration in [Paper VII] and [Paper VIII] are equipped with in-wheel motors that are mounted on all four corners of the vehicle. It is also assumed that each wheel is equipped with two linear actuators that can move symmetrically around the vertical axis of the wheel, thereby providing arbitrary steering angles (within a specified interval). Furthermore, each wheel hub is also equipped with mechanical friction brakes to provide braking power at levels that cannot regenerate through the in-wheel motors.

¹The term *machine* is perhaps more appropriate since power can be generated during braking. However, the term is less common in this context and, therefore, not used here.

²The synonym ultracapacitor is also commonly used.

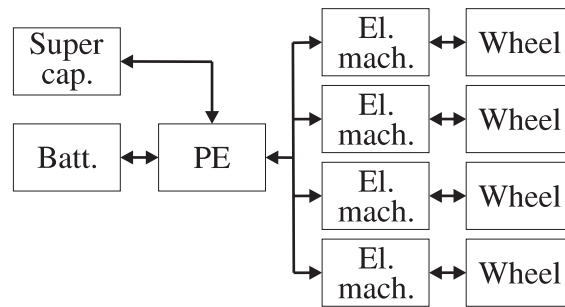


Fig. 4.7 Flowchart of the drivetrain considered in the case studies in [Paper VII] and [Paper VIII]. The arrows indicate possible directions of energy flow.

Consequently, each wheel corner is capable of providing individual propulsion or braking power and control of the steering angle. The described configuration originates from the *autonomous corner module* (ACM), a device that, apart from providing individual propulsion/braking power and control of the steering angle, can also control the vertical load and damping coefficients on each wheel (the ACM is further described in [44] and [79]). Active control of the vertical dynamics are not taken into consideration here. However, it may very well be needed due to the fact that the use of in-wheel motors increases the *unsprung mass* which, if not compensated for, worsens the response of the car body to road irregularities up to levels which may seriously affect passenger comfort.

An illustration of the main parts of the electric drivetrain considered is shown in Fig. 4.8 where the linear actuators controlling the individual steering angles have been omitted. Four inverters provide individual control of each in-wheel motor. The supercapacitor is, in series with a filter inductor, connected in parallel to the battery through a dc/dc-converter of buck/boost type (the voltage across the supercapacitor is always lower than the dc-link voltage). By controlled switching of the upper or lower transistor of the dc/dc-converter, power can be fed to or from the supercapacitor. In a practical application, the power consumption of the battery and supercapacitor are governed by some kind of *energy-management strategy* whose overall goal typically is to minimize the total energy consumption of the vehicle, evaluated using a number of relevant driving cycles. Examples of such energy-management strategies can be found in, e.g., [2] and [28].

4.5.2 Simulation Study

A simulation model of the electric drivetrain shown in Fig. 4.8 was implemented using Matlab/Simulink³ in combination with the PLECS⁴ toolbox to simulate the switching states of the power electronics. The switching frequency of the inverters was set to 10 kHz. A flow chart of the simulation structure is shown in Fig. 4.9. Since the vehicle was equipped with four individual drives, the additional cost to provide fault tolerance

³Simulink is a registered trademark of The Mathworks, Inc., Natick, Massachusetts, U.S.A.

⁴PLECS is a registered trademark of Plexim GmbH, Zürich, Switzerland.

4.5. Electrical Faults in a Propulsion Application

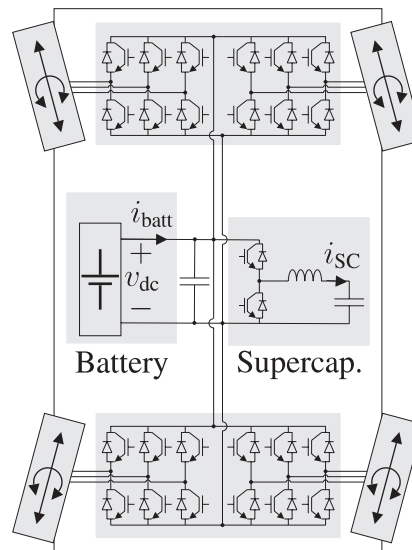


Fig. 4.8 Illustration of the electric drivetrain for the vehicle in consideration. The linear actuators controlling the individual steering angles on each wheel are not shown.

for each of the drives will likely be very expensive, subsequently such a solution is not considered here.

In the present simulation study, it is assumed that all four inverters are individually controlled and that they are equipped with IPM modules that, in the event of an electrical fault, gate off the transistors, thereby causing an inverter shutdown. Reasons for the origin of such an inverter shutdown include failure of the control-supply voltage that powers the IPM module, a local failure in the gate drive, and a signal-cable breakdown.

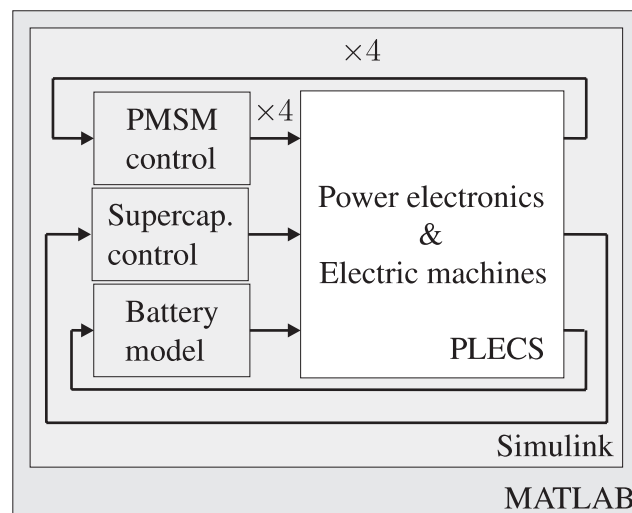


Fig. 4.9 Schematic flow chart of the simulation structure used. Arrows indicate feedback signals used in the closed-loop controllers and battery model.

The simulation of inverter switches is realized in PLECS using PWM with sym-

metrical, triangular carriers. Naturally, this requires a much smaller time step than used in the outer controllers, which are updated once every switching period. The parameters of the four electric machines correspond to PMSM2 and their current controllers are implemented in discrete form in Simulink, using S-functions. The parameters of the supercapacitor and corresponding filter inductor are chosen from [21] which presents a supercapacitor and battery combination implemented in an EV. The total capacitance and series resistance of the supercapacitor are 20 F and 125 m Ω , respectively. The inductance of the filter inductor is 1.6 mH and it has a total series resistance of 30 m Ω . The power flow in the supercapacitor is controlled by closed-loop control of the supercapacitor current using a PI controller whose parameters are determined in a fashion similar to the description in Section 2.4.1.

The battery model, implemented in Simulink, represents a Lithium-ion battery⁵ and is similar to the capacitor-network models presented in [15] and [27]. The minimum and maximum battery voltages allowed are 240 and 400 V, respectively. To filter the inverter ripple currents, a dc-link capacitor with a capacitance of 6.6 mF was adopted.

In the hypothetical driving situation considered here, all four PMSMs operate at a constant (mechanical) speed of 90 rad/s which corresponds to approximately 104 km/h if a tire radius of 0.32 m is assumed and the longitudinal tire slip is neglected (recall that PMSM2 is an outer-rotor machine where the rotor magnets are mounted directly onto the wheel rim). All four PMSMs deliver a total of 26 kW which is evenly distributed on each wheel. The power is taken purely from the battery, i.e., no current flows initially in the supercapacitor. Due to the relatively high rotor speed, all four PMSMs operate in the field-weakening region at the operating point $i_d = -40$, $i_q = 20$ A. At $t = 5$ ms, one of the inverters controlling an in-wheel motor shuts down, and starts to generate power into the dc link.

Fig. 4.10 shows results from the corresponding simulation where the supercapacitor is controlled so that the battery current is essentially unaffected by the fault. Subsequently, the supercapacitor absorbs not only the power that is generated from the faulted PMSM drive, but also the amount of power that it consumed before the inverter shutdown. The remaining PMSM drives are, therefore, virtually unaffected by the fault and fully controllable. The control strategy of the supercapacitor used in this simulation is very simple and is only adopted for the purpose of illustration.

As described in Section 4.3, an inverter shutdown striking one of the inverters results in a sudden, speed dependent, braking torque. The question of whether or not the arising braking torque affects passenger safety is strongly dependent on vehicle dynamics, i.e., how the vehicle responds to the fault. The fact that the remaining in-wheel motors are still operable provides the possibility for an “in-built” fault tolerance to this type of electrical fault for the vehicle in consideration. Moreover, if the battery is not able to

⁵The author is grateful to Mr. Jens Groot at Volvo Technology Corporation, Göteborg, Sweden for supplying the battery model.

quickly generate, or absorb, the power that may be needed for rapid counteractions by the remaining, fully functioning, in-wheel motors, this power can be generated, or absorbed, by the supercapacitor.

It is apparent that the fault scenario described above, along with a wide range of other fault scenarios comprising electrical faults, is of importance and should be taken into consideration before a vehicle using the described electric drivetrain leaves the prototype stage. In [Paper VII] and [Paper VIII], the stability of a vehicle equipped with the electric drivetrain shown in Fig. 4.10 is investigated under different types of fault conditions and driving scenarios. Since the drivetrain provides individual control of both torque and the steering angle on each wheel, the tire forces can be distributed freely on each wheel, which offers the possibility to counteract a faulted in-wheel motor by modifying the tire forces on the remaining, still functioning, wheels.

4.6 Summary of Chapter

This chapter focused on various implications of electrical faults striking PMSM drives in automotive applications. Electric machines and inverters that provide means for fault tolerance were described and the response of PMSMs to inverter faults was illustrated through simulations. Finally, the impact of an electrical fault in a propulsion application was considered in the form of a simulation study which also serves as a background for the case studies presented in [Paper VII] and [Paper VIII].

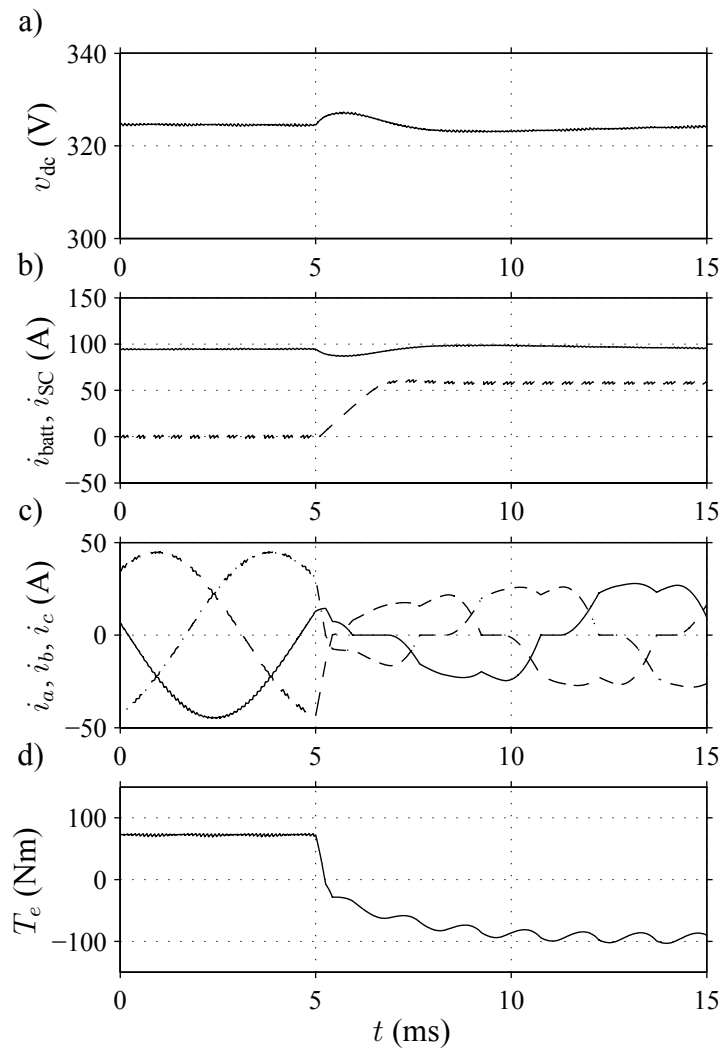


Fig. 4.10 Simulation of an inverter shutdown at one wheel for the electric drivetrain illustrated in Fig. 4.8: a) Battery voltage; b) Battery (solid line) and supercapacitor (dashed line) currents; c) Phase currents of the faulted PMSM: i_a (solid line), i_b (dashed line), and i_c (dashed-dotted line); d) Torque of the faulted PMSM.

Chapter 5

Concluding Remarks

This chapter summarizes conclusions and provides some suggestions for further research related to the different topics considered in this thesis.

5.1 Summary

This thesis presented control algorithms for PMSM drives that can be applied to a wide range of automotive applications. Adopting highly efficient PMSMs for propulsion and also using them in other electrically assisted functions can help to maximize the operating range and (for HEVs) minimize the fuel consumption.

Sensorless control of PMSM drives offers obvious advantages in terms of cost, size, and reliability and was explored extensively in this thesis. Since this field of research is mature, focus was not on presenting entirely novel methods but rather on analyzing and proposing improvements to already existing solutions. Several modifications to the PLL-type estimator reported in [32] were proposed. Based on an analysis of the *global* stability of the original estimator, a method was presented that improves the estimator's capability to handle large speed estimation errors, arising, e.g., during rapid accelerations of short duration or during an initiation of the estimator at an unknown speed. To achieve stable operation in the whole speed range, it was demonstrated how the estimator could incorporate signal-injection based estimation in the low-speed range with a transition to back-EMF based estimation at higher speeds. Particular focus was also on the transition region and it was demonstrated that the estimator may become unstable for certain setups of machine parameters and operating conditions if the transition region is determined incorrectly. To avoid this instability, design rules for how the transition region should be determined, as well as recommended selections for all parameters introduced were presented.

Signal-injection based estimation for PMSMs with small rotor saliency is difficult since the signal-to-noise ratio can be very small and additional non-ideal effects, such as inverter dead time and inductance cross saturation, become significant. The back-EMF

based estimator based on the well known “voltage model” is suitable for a wide range of applications where high performance in the low-speed region is not critical as long as a startup and possibly also rotation reversals can be guaranteed. The estimator is, due to its simplicity, robustness to parameter variations, and global stability properties, of particular interest for applications where accurate knowledge of machine parameters is lacking and careful tuning of the estimator is not possible, e.g., in commercial inverter drives.

In summary, the analysis of the estimators in consideration has highlighted several important phenomena and the improvements presented simplify a possible implementation considerably; particularly since parameter selection rules for all estimator parameters are proposed as a result of the analysis.

The severity of faults striking electric drives in automotive applications is strongly dependent on how they affect the passenger safety. Several subsystems, including steer- and brake-by-wire systems, have not yet been introduced on a large scale in commercial vehicles. Hence, although it is evident that the failure of any of these functions is very critical in terms of passenger safety, it is not clear, at this stage, exactly what levels of fault tolerance will be required. The control algorithms presented for the fault-tolerant PMSM drive provide simple modifications that extend its capability. If fault tolerance is required for inverter and winding open-circuit faults, the fault-tolerant PMSM drive in consideration, in combination with the proposed control algorithms can be a viable solution.

The investigations concerning the impact of various electrical faults in vehicles equipped with four in-wheel motors provide several important insights related to how electrical faults in novel drivetrains can affect vehicle stability. It is evident that a comprehensive knowledge concerning these issues is of importance and should be taken into consideration during the design stage of modern electric drivetrains. The investigations also demonstrate that individual control of the tire forces provides powerful means for an “in-built” fault tolerance capable of handling a wide range of electrical faults with only minor displacements from the intended driving trajectory.

5.2 Proposals for Future Work

In this thesis, control algorithms for PMSM drives were presented with automotive applications in mind. Some ideas for further research in this and related fields are outlined below.

Regarding sensorless control of PMSM drives, design guidelines should be developed and, to a greater extent than today, be incorporated into the design stage of PMSMs, intended for automotive applications, in order to guarantee that signal-injection based estimation methods can be easily applied. Another interesting topic related to this field is to investigate whether or not the back-EMF based estimator presented in [Paper IV] can be further improved so that the noise content of the estimates at low speeds, and tran-

sient error at rotation reversal can be reduced. However, it is important that the attractive properties of the estimator, including low parameter sensitivity and ease of implementation, are maintained so that the algorithm can remain suitable for applications such as commercial inverter drives.

The investigation into electrical faults in a vehicle equipped with four in-wheel motors should only be considered as a first step and more research and development are required for issues related to this field. An implementation of the electric drivetrain in a laboratory environment can provide answers to how the power should be redistributed in the drivetrain in the event of an electrical fault. Implementing the drivetrain into a vehicle, a scale or full-scale prototype, would also provide useful experimental data on how the path controller and various force-allocation methods respond to different driving conditions and electrical faults. Another interesting issue would be to investigate whether or not a transient rise in dc-link voltage during a high-speed inverter shutdown can always be avoided by rapidly diverting the generated power into the supercapacitor. This is attractive since it would enable the use of IGBTs with a lower margin in terms of voltage rating.

Since electric machines and power electronics are key components in electric and hybrid electric drivetrains, this offers good opportunities for further research in the field of electric drives. However, the quest for tomorrow's alternative drivetrains is, by nature, multi-disciplinary and research activities belonging to several other scientific fields, including chemistry, mechanical engineering, and vehicle dynamics, are currently ongoing or being planned. On the national level, it is the opinion of the author that more extended coordination and cooperation between different departments *within* the universities are needed in order to further strengthen university-based research related to alternative drivetrains. Today, this is, to some extent, hindered due to the organizational structures within the universities. Sweden has several vehicle manufacturers and better coordination within the universities themselves would enable researchers from academia to carry out multi-disciplinary research in a more systematic and efficient manner which hopefully would lead to more breakthroughs and results of interest for the automotive industry.

Chapter 5. Concluding Remarks

References

- [1] P. P. Acarnley and J. F. Watson, "Review of position-sensorless operation of brushless permanent-magnet machines," *IEEE Trans. Ind. Electron.*, vol. 53, no. 2, pp. 352–362, Apr. 2006.
- [2] T. Andersson and J. Grooth, "Alternative energy storage system for hybrid electric vehicles," Master's thesis, Chalmers Univ. Technol., Göteborg, Sweden, Oct. 2003.
- [3] A. Arias, C. A. Silva, G. M. Asher, J. C. Clare, and P. W. Wheeler, "Use of a matrix converter to enhance the sensorless control of a surface-mount permanent-magnet AC motor at zero and low frequency," *IEEE Trans. Ind. Electron.*, vol. 53, no. 2, pp. 440–449, Apr. 2006.
- [4] J. W. Bennet, A. G. Jack, B. C. Mecrow, D. J. Atkinson, C. Sewell, and G. Mason, "Fault-tolerant control architecture for an electrical actuator," in *Proc. IEEE 35th Power Electron. Specialists Conf.*, vol. 6, 2004, pp. 4371–4377.
- [5] B. S. Bhangu and C. M. Bingham, "GA-tuning of nonlinear observers for sensorless control of automotive power steering IPMSMs," in *Proc. IEEE Vehicle Power and Propulsion Conf.*, 2005, pp. 772–779.
- [6] N. Bianchi and S. Bolognani, "Fault-tolerant PM motors in automotive applications," in *Proc. IEEE Vehicle Power and Propulsion Conf.*, 2005, pp. 747–755.
- [7] N. Bianchi, S. Bolognani, and M. Zigliotto, "Innovative remedial strategies for inverter faults in IPM synchronous motor drives," *IEEE Trans. Energy Conversion*, vol. 18, no. 2, pp. 306–314, June 2003.
- [8] ———, "Design hints of an IPM synchronous motor for an effective position sensorless control," in *Proc. IEEE 36th Power Electron. Specialists Conf.*, 2005, pp. 1560–1566.
- [9] S. Bolognani, R. Oboe, and M. Zigliotto, "Sensorless full-digital PMSM drive with EKF estimation of speed and rotor position," *IEEE Trans. Ind. Electron.*, vol. 46, no. 1, pp. 184–190, Feb. 1999.

References

- [10] S. Bolognani, M. Zordan, and M. Zigliotto, "Experimental fault-tolerant control of a PMSM drive," *IEEE Trans. Ind. Electron.*, vol. 47, no. 5, pp. 1134–1141, Oct. 2000.
- [11] J. Bonet-Madurga and A. Díez-González, "Modelling of permanent magnet synchronous motors with spatial harmonics," *European Trans. on Electrical Power*, vol. 12, no. 5, pp. 369–375, Sept./Oct. 2002.
- [12] S. G. Bosga, "Assymetrical supply of induction machines," Ph.D. Dissertation, Technische Universiteit Eindhoven, Eindhoven, The Netherlands, May 1997.
- [13] F. Briz, M. W. Degner, and R. D. Lorenz, "Analysis and design of current regulators using complex vectors," *IEEE Trans. Ind. Applicat.*, vol. 36, no. 3, pp. 817–825, May/June 2000.
- [14] W. Cai, "Comparison and review of electric machines for integrated starter alternator applications," in *Conf. Rec. IEEE 39th IAS Annu. Meeting*, vol. 1, 2004, pp. 386–393.
- [15] A. Capel, "Mathematical model for the representation of the electrical behaviour of a lithium cell," in *Proc. IEEE 32nd Power Electron. Specialists Conf.*, vol. 4, 2001, pp. 1976–1981.
- [16] C. Cavallaro, A. O. Di Tommaso, R. Miceli, A. Raciti, G. R. Galluzzo, and M. Trapanese, "Efficiency enhancement of permanent-magnet synchronous motor drives by online loss minimization approaches," *IEEE Trans. Ind. Electron.*, vol. 52, no. 4, pp. 1153–1160, Aug. 2005.
- [17] C. C. Chan and Y. S. Wong, "The state of the art of electric vehicles technology," in *Proc. 4th Int. Conf. Power Electron. and Motion Control*, vol. 1, 2004, pp. 46–57.
- [18] M. Ciappa, F. Carbognani, and W. Fichtner, "Lifetime prediction and design of reliability tests for high-power devices in automotive applications," *IEEE Trans. Device Mat. Rel.*, vol. 3, no. 4, pp. 191–196, Dec. 2003.
- [19] M. J. Corley and R. D. Lorenz, "Rotor position and velocity estimation for a salient-pole permanent magnet synchronous machine at standstill and high speeds," *IEEE Trans. Ind. Applicat.*, vol. 34, no. 4, pp. 784–789, July/Aug. 1998.
- [20] D. Diallo, M. E. H. Benbouzid, and A. Makouf, "A fault-tolerant control architecture for induction motor drives in automotive applications," *IEEE Trans. Veh. Technol.*, vol. 53, no. 6, pp. 1847–1855, Nov. 2004.
- [21] J. W. Dixon and M. E. Ortúzar, "Ultracapacitors + DC-DC converters in regenerative braking system," *IEEE/AESS Systems Mag.*, vol. 17, no. 8, pp. 16–21, Aug. 2002.

- [22] A. M. EL-Refaie and T. M. Jahns, "Comparison of synchronous PM machine types for wide constant-power speed range operation," in *Conf. Rec. IEEE 40th IAS Annu. Meeting*, vol. 2, 2005, pp. 1015–1022.
- [23] A. Emadi, S. S. Williamson, and A. Khaligh, "Power electronics intensive solutions for advanced electric, hybrid electric, and fuel cell vehicular power systems," *IEEE Trans. Power Electron.*, vol. 21, no. 3, pp. 567–577, May 2006.
- [24] J. Faiz, M. B. B. Sharifian, A. Keyhani, and A. B. Proca, "Sensorless direct torque control of induction motors used in electric vehicle," *IEEE Trans. Energy Conversion*, vol. 18, no. 1, pp. 1–10, Mar. 2003.
- [25] T. Frenzke, "Impacts of cross-saturation on sensorless control of surface permanent magnet synchronous motors," in *Proc. 11th European Conf. Power Electron. and Applicat.*, 2005.
- [26] A. Fukuma, S. Kanazawa, D. Miyagi, and N. Takahashi, "Investigation of AC loss of permanent magnet of SPM motor considering hysteresis and eddy-current losses," *IEEE Trans. Magn.*, vol. 41, no. 5, pp. 1964–1967, May 2005.
- [27] L. Gao, S. Liu, and R. A. Dougal, "Dynamic lithium-ion battery model for system simulation," *IEEE Trans. Comp. Packag. Technol.*, vol. 25, no. 3, pp. 495–505, Sept. 2002.
- [28] M. J. Gielniak and Z. J. Shen, "Power management strategy based on game theory for fuel cell hybrid electric vehicles," in *Proc. IEEE 60th Vehicular Technol. Conf.*, vol. 6, 2004, pp. 4422–4426.
- [29] S. Green, D. J. Atkinson, A. G. Jack, B. C. Mecrow, and A. King, "Sensorless operation of a fault tolerant PM drive," *IEE Proc. Electric Power Applicat.*, vol. 150, no. 2, pp. 117–125, Mar. 2003.
- [30] P. Guglielmi, M. Pastorelli, and A. Vagati, "Cross saturation effects in IPM motors and related impact on zero-speed sensorless control," in *Conf. Rec. IEEE 40th IAS Annu. Meeting*, vol. 4, 2005, pp. 2546–2552.
- [31] M. C. Harke, D. Raca, and R. D. Lorenz, "Implementation issues for fast initial position and magnet polarity identification of PM synchronous machines with near zero saliency," in *Proc. 11th European Conf. Power Electron. and Applicat.*, 2005.
- [32] L. Harnefors and H.-P. Nee, "A general algorithm for speed and position estimation of AC motors," *IEEE Trans. Ind. Electron.*, vol. 47, no. 1, pp. 77–83, Feb. 2000.

References

- [33] L. Harnefors, K. Pietiläinen, and L. Gertmar, “Torque-maximizing field-weakening control: design, analysis, and parameter selection,” *IEEE Trans. Ind. Electron.*, vol. 48, no. 1, pp. 161–168, Feb. 2001.
- [34] J. Hellsing, “Design and optimization of a permanent magnet motor for a hybrid electric vehicle,” Licentiate Thesis, Chalmers Univ. Technol., Göteborg, Sweden, Mar. 1998.
- [35] J. R. Hendershot and T. J. E. Miller, *Design of Brushless Permanent-Magnet Motors*. Oxford, U.K.: Magna Physics Publishing and Clarendon Press, 1994.
- [36] D. Hirschmann, D. Tissen, S. Schröder, and R. W. De Doncker, “Reliability prediction for inverters in hybrid electrical vehicles,” in *Proc. IEEE 37th Power Electron. Specialists Conf.*, 2006.
- [37] K. H. Hussein, G. Majumdar, S. Yoshida, and H. Maekawa, “IPMs solving major reliability issues in automotive applications,” in *Proc. 17th Int. Symp. Power Semiconductor Devices and ICs*, 2005, pp. 89–92.
- [38] S. Ichikawa, M. Tomita, S. Doki, and S. Okuma, “Sensorless control of permanent-magnet synchronous motors using online parameter identification based on system identification theory,” *IEEE Trans. Ind. Electron.*, vol. 53, no. 2, pp. 363–372, Apr. 2006.
- [39] N. Imai, S. Morimoto, M. Sanada, and Y. Takeda, “Influence of PM flux variation and magnetic saturation on sensorless control for interior permanent magnet synchronous motors,” in *Conf. Rec. IEEE 40th IAS Annu. Meeting*, vol. 3, 2005, pp. 1776–1783.
- [40] K. Ishikawa, K. Suda, M. Sasaki, and H. Miyazaki, “A 600V driver IC with new short protection in hybrid electric vehicle IGBT inverter system,” in *Proc. 17th Int. Symp. Power Semiconductor Devices and ICs*, 2005, pp. 59–62.
- [41] T. M. Jahns and V. Caliskan, “Uncontrolled generator operation of interior PM synchronous machines following high-speed inverter shutdown,” *IEEE Trans. Ind. Applicat.*, vol. 35, no. 6, pp. 1347–1356, Nov./Dec. 1997.
- [42] J.-H. Jang, S.-K. Sul, J.-I. Ha, K. Ide, and M. Sawamura, “Sensorless drive of surface-mounted permanent-magnet motor by high-frequency signal injection based magnetic saliency,” *IEEE Trans. Ind. Applicat.*, vol. 39, no. 4, pp. 1031–1039, July/Aug. 2003.
- [43] Y.-S. Jeong, S.-K. Sul, S. E. Schulz, and N. R. Patel, “Fault detection and fault-tolerant control of interior permanent-magnet motor drive system for electric vehicle,” *IEEE Trans. Ind. Applicat.*, vol. 41, no. 1, pp. 46–51, Jan./Feb. 2005.

- [44] M. Jonasson, S. Zetterström, and A. S. Trigell, “Autonomous corner modules as an enabler for new vehicle chassis solutions,” to be presented at the *31st FISITA World Automotive Congress*.
- [45] W. D. Jones, “Hybrids to the rescue [hybrid electric vehicles],” *IEEE Spectr.*, vol. 40, no. 1, pp. 70–71, Jan. 2003.
- [46] M. P. Kazmierkowski, R. Krishnan, and F. Blaabjerg, Eds., *Control in Power Electronics—Selected Problems*. London, U.K.: Academic Press, 2002.
- [47] J.-M. Kim and S.-K. Sul, “Speed control of interior permanent magnet synchronous motor drive for the flux weakening operation,” *IEEE Trans. Ind. Applicat.*, vol. 33, no. 1, pp. 43–48, Jan./Feb. 1997.
- [48] P. C. Krause, O. Wasynczuk, and S. D. Sudhoff, *Analysis of Electric Machinery and Drive Systems*. Piscataway, NJ: IEEE Press, 1994.
- [49] M. Linke, R. Kennel, and J. Holtz, “Sensorless speed and position control of synchronous machines using alternating carrier injection,” in *Proc. IEEE 4th Int. Conf. Electric Machines and Drives*, vol. 2, 2003, pp. 1211–1217.
- [50] T. H. Lio, J. R. Fu, and T. A. Lipo, “A strategy for improving reliability of field-oriented induction motor drives,” *IEEE Trans. Ind. Applicat.*, vol. 29, no. 5, pp. 910–918, Sept./Oct. 1993.
- [51] C. Mademlis, I. Kioskeridis, and N. Margaris, “Optimal efficiency control strategy for interior permanent-magnet synchronous motor drives,” *IEEE Trans. Energy Conversion*, vol. 19, no. 4, pp. 715–723, Dec. 2004.
- [52] R. Masaki, S. Kaneko, M. Hombu, T. Sawada, and S. Yoshihara, “Development of a position sensorless control system on an electric vehicle driven by a permanent magnet synchronous motor,” in *Proc. Power Conversion Conf.*, vol. 2, 2002, pp. 571–576.
- [53] N. Matsui, “Sensorless PM brushless DC motor drives,” *IEEE Trans. Ind. Electron.*, vol. 43, no. 2, pp. 300–308, Apr. 1996.
- [54] B. C. Mecrow, A. G. Jack, D. J. Atkinson, S. R. Green, G. J. Atkinson, A. King, and B. Green, “Design and testing of a four-phase fault-tolerant permanent-magnet machine for an engine fuel pump,” *IEEE Trans. Energy Conversion*, vol. 19, no. 4, pp. 671–677, Dec. 2004.
- [55] B. C. Mecrow, A. G. Jack, J. A. Haylock, and J. Coles, “Fault-tolerant permanent magnet machine drives,” *IEE Proc. Electric Power Applicat.*, vol. 143, no. 6, pp. 437–442, Nov. 1996.

References

- [56] P. H. Mellor, T. J. Allen, R. Ong, and Z. Rahman, "Faulted behaviour of permanent magnet electric vehicle traction drives," in *Proc. IEEE 4th Int. Conf. Electric Machines and Drives*, vol. 1, 2003, pp. 554–558.
- [57] B. N. Mobarakeh, F. Meibody-Tabar, and F. M. Sargos, "A globally converging observer of mechanical variables for sensorless PMSM," in *Proc. IEEE 31st Power Electron. Specialists Conf.*, vol. 2, 2000, pp. 885–890.
- [58] A. Morozumi, K. Yamada, T. Miyasaka, S. Sumi, and Y. Seki, "Reliability of power cycling for IGBT power semiconductor modules," *IEEE Trans. Ind. Appl. cat.*, vol. 39, no. 3, pp. 665–671, May/June 2003.
- [59] E. R. Motto and J. F. Donlon, "Speed shifting gate drive for intelligent power modules," in *Proc. IEEE 21st Applied Power Electron. Conf. and Exp.*, 2006, pp. 1684–1690.
- [60] M. Naidu, T. W. Nehl, S. Gopalakrishnan, and L. Würth, "Keeping cool while saving space and money: a semi-integrated, sensorless PM brushless drive for a 42-V automotive HVAC compressor," *IEEE Ind. Appl. Mag.*, vol. 11, no. 4, pp. 20–28, July/Aug. 2005.
- [61] M. A. Redfern and M. J. Checksfield, "A review of pole slipping protection," in *IEE Colloquium on Gen. Prot.*, 1996, pp. 6/1–6/9.
- [62] L. A. S. Ribeiro, M. C. Harke, and R. D. Lorenz, "Dynamic properties of back-EMF based sensorless drives," to be presented at the *IEEE 41st IAS Annu. Meeting*.
- [63] R. L. A. Riberio, C. B. Jacobina, E. R. C. da Silva, and A. M. N. Lima, "Fault-tolerant voltage-fed PWM inverter AC motor drive systems," *IEEE Trans. Ind. Electron.*, vol. 51, no. 2, pp. 439–446, Apr. 2004.
- [64] V. A. Sankaran, C. Chen, C. S. Avant, and X. Xu, "Power cycling reliability of IGBT power modules," in *Conf. Rec. IEEE 32nd IAS Annu. Meeting*, vol. 2, 1997, pp. 1222–1227.
- [65] R. H. Schallenberg, "Prospects for the electric vehicle: a historical perspective," *IEEE Trans. Educ.*, vol. E-23, no. 3, pp. 137–143, Aug. 1980.
- [66] M. Schroedl, "Sensorless control of AC machines at low speed and standstill based on the "INFORM" method," in *Conf. Rec. IEEE 31st IAS Annu. Meeting*, vol. 1, 1996, pp. 270–277.
- [67] —, "Sensorless control of permanent magnet synchronous machines: an overview," in *Proc. EPE 11th Int. Conf. Power Electron. and Motion Control*, 2004.

- [68] T. Senjyu, N. Urasaki, T. Kinjo, and H. Sekine, "Parameter measurement for surface-mounted permanent magnet synchronous motor taking stator iron loss into account," *Electric Power Components and Systems*, vol. 33, no. 11, pp. 1237–1251, Nov. 2005.
- [69] S. Shinnaka and S. Takeuchi, "Development of sensorless-vector-controlled and transmissionless EV using a high efficient permanent magnet synchronous motor," in *Proc. SICE 4th Annu. Conf. Control Systems*, 2004, pp. 571–574.
- [70] C. Silva, G. M. Asher, and M. Sumner, "Hybrid rotor position observer for wide speed-range sensorless PM motor drives including zero speed," *IEEE Trans. Ind. Electron.*, vol. 53, no. 2, pp. 373–378, Apr. 2006.
- [71] J. L. Stensby, *Phase-Locked Loops: Theory and Applications*. Boca Raton, FL: CRC Press, 1997.
- [72] C. Sulzberger, "Early road warrior, part 2 – competing electric and gasoline vehicles," *IEEE Power Energy Mag.*, vol. 2, no. 5, pp. 83–88, Sept./Oct. 2004.
- [73] J. Wai and T. M. Jahns, "A new control technique for achieving wide constant power speed operation with an interior PM alternator machine," in *Conf. Rec. IEEE 36th IAS Annu. Meeting*, vol. 2, 2001, pp. 807–814.
- [74] O. Wallmark, "On control of permanent-magnet synchronous motors in hybrid-electric vehicle applications," Licentiate Thesis, Chalmers Univ. Technol., Göteborg, Sweden, Mar. 2004.
- [75] B. A. Welchko, T. M. Jahns, and S. Hiti, "IPM synchronous machine drive response to a single-phase open circuit fault," *IEEE Trans. Power Electron.*, vol. 17, no. 5, pp. 764–771, Sept. 2002.
- [76] B. A. Welchko, T. M. Jahns, W. L. Soong, and J. M. Nagashima, "IPM synchronous machine drive response to symmetrical and asymmetrical short circuit faults," *IEEE Trans. Energy Conversion*, vol. 18, no. 2, pp. 291–298, June 2003.
- [77] B. A. Welchko, T. A. Lipo, T. M. Jahns, and S. E. Schultz, "Fault tolerant three-phase AC motor drive topologies: a comparison of features, costs, and limitations," *IEEE Trans. Power Electron.*, vol. 19, no. 4, pp. 1108–1116, July 2004.
- [78] L. Ying and N. Ertugrul, "A novel, robust DSP-based indirect rotor position estimation for permanent magnet AC motors without rotor saliency," *IEEE Trans. Power Electron.*, vol. 18, no. 2, pp. 539–546, Mar. 2003.
- [79] S. Zetterström, "Electromechanical steering, suspension, drive and brake modules," in *Proc. IEEE 56th Vehicular Technol. Conf.*, vol. 3, 2002, pp. 1856–1863.

References

Appendix A

Glossary of Symbols, Subscripts, Superscripts, and Abbreviations

Symbols

A	system matrix
B	input matrix
B_r	radial flux density
b	damping constant
E	disturbance matrix
G, \mathbf{G}	transfer function and transfer function matrix
I	identity matrix
I	integration state
i, \mathbf{i}	current and current vector
J	rotational matrix, $\mathbf{J} = \begin{bmatrix} 0 & -1 \\ 1 & 0 \end{bmatrix}$
J	inertia
j	imaginary unit, $\sqrt{-1}$
k_i	integration gain
k_p	proportional gain
L, \mathbf{L}	inductance and inductance matrix
l_s	active length of stator
N	turn distribution
n_p	number of pole pairs
p	d/dt
R	resistance
r_s	inner radius of stator
S, \mathbf{S}	sensitivity function and sensitivity-function matrix
$\mathbf{T}_{dq,ph}$	Park transformation matrix
T_e	electro-mechanical torque

Appendix A. Glossary of Symbols, Subscripts, Superscripts, and Abbreviations

T_l	load torque
t	time
t_r	rise time
V	voltage
v, \mathbf{v}	voltage and voltage vector
\mathbf{W}	decoupling transfer function matrix
W_{co}	coenergy
\mathbf{x}	state vector
\mathbf{Z}	impedance matrix
α	bandwidth
γ	gain constant
ΔL	$\Delta L = L_q - L_d$
θ	electrical rotor angle (position)
ϑ	rotor magnet angle
λ	gain constant
ν	disturbance vector
ρ	gain constant
ϱ	conductor-density distribution angle
ψ, Ψ	flux linkage and flux linkage vector
ω_r	electrical rotor speed
\triangleq	equals by definition
\cdot	d/dt
$\hat{}$	estimated
\sim	error

Subscripts

a	active damping or phase a component
b	phase b component
c	core, current or phase c component
cl	closed loop
d	direct-axis component
fric	friction
l	load
m	magnet or mutual
mech	mechanical
ph	phase quantity
q	quadrature-axis component
r	rotor
s	self (inductance), speed or stator
0	zero component

Superscripts

ref	reference
T	transpose of matrix/vector
*	equilibrium point

Abbreviations

ACM	autonomous corner module
Batt.	battery
BLDC	brushless dc (machine)
DSP	digital signal processor
det	determinant
diag	diagonal (matrix)
El. mach.	electric machine
EMF	electromotive force
EV	electric vehicle
FCV	fuel-cell vehicle
Gen.	generator
HEV	hybrid electric vehicle
ICE	internal combustion engine
IGBT	insulated gate bipolar transistor
IMC	internal model control
IPM	intelligent power module
MTPA	maximum torque-per-ampere
PD	phase detector
PE	power electronics
PI	proportional plus integral
PLL	phase-locked loop
PMSM	permanent-magnet synchronous machine
PWM	pulse width modulation
pu	per unit
ref	reference
rms	root mean square
Super cap.	supercapacitor
Trans.	transmission

Appendix A. Glossary of Symbols, Subscripts, Superscripts, and Abbreviations

Appendix B

Adopted Per-Unit System and PMSM Parameters

B.1 Per-Unit System

The base values of the per-unit system used in the present thesis are given in Table B.1. The system is intended for an inverter-fed PMSM with a permanent-magnet flux linkage ψ_m and a rated (rms) phase current I_n . The dc-link voltage v_{dc} is used as base voltage.

Table B.1: Base values of the per-unit system.

Base value	Definition
Base voltage	$v_{\text{base}} = \frac{v_{\text{dc}}}{\sqrt{3}}$
Base current	$i_{\text{base}} = \sqrt{2}I_n$
Base angular frequency	$\omega_{\text{base}} = \frac{v_{\text{base}}}{\psi_m}$

B.2 PMSM Parameters

B.2.1 PMSM1

PMSM1 refers to a PMSM adopting an inner-rotor design with inset-mounted magnets and is developed for propulsion in a series-HEV. The machine is Y-connected, the maximum continuous output power is 50 kW, and the intended dc-link voltage is 320 V which

Appendix B. Adopted Per-Unit System and PMSM Parameters

corresponds to an electrical base speed (calculated according to Table B.1) of approximately 1780 rad/s. For further details concerning PMSM1, see [34].

Table B.2: Data for PMSM1 (cold condition).

Connection	Y	
No. of pole pairs	n_p	2
Rated current	I_n	160 A
Stator res. ($f=0$ Hz)	R_s	7.9 m Ω
d -axis inductance	L_d	0.23 mH
q -axis inductance ($i_q=0$ pu)	L_q	0.56 mH
q -axis inductance ($i_q=1$ pu)	L_q	0.42 mH
Permanent-magnet flux linkage	ψ_m	104 mWb

B.2.2 PMSM2

PMSM2 refers to an experimental in-wheel motor adopting an outer-rotor design with surface-mounted magnets mounted directly onto the wheel rim. The PMSM has been designed by Dr. A. Grauers, currently at Volvo Cars Corporation. If the dc-link voltage is 400 V, the wheel radius is 0.32 m, and the longitudinal tire slip is neglected, the base speed corresponds to a vehicle speed of approximately 105 km/h.

Table B.3: Data for PMSM2 (cold condition).

Connection	Y	
No. of pole pairs	n_p	8
Rated current	I_n	52 A
Stator res. ($f=0$ Hz)	R_s	160 m Ω
d -axis inductance	L_d	2.5 mH
q -axis inductance	L_q	2.9 mH
Permanent-magnet flux linkage	ψ_m	318 mWb

Appendix C

Selected Publications

Paper I

O. Wallmark, L. Harnefors, and O. Carlson, "An improved speed and position estimator for salient permanent-magnet synchronous motors," *IEEE Transactions on Industrial Electronics*, vol. 52, no. 1, pp. 255-262, Feb. 2005.

I

Paper II

O. Wallmark, L. Harnefors, and O. Carlson, "Sensorless control of PMSM drives for hybrid electric vehicles," in *Proc. 35th Annual IEEE Power Electronics Specialists Conference (IEEE PESC '04)*, vol. 5, 2004, pp. 4017–4023.



© 2004 IEEE. Reprinted with permission.

Paper III

O. Wallmark and L. Harnefors, "Sensorless control of salient PMSM drives in the transition region," *IEEE Transactions on Industrial Electronics*, vol. 53, no. 4, pp. 1179-1187, Aug. 2006.



© 2006 IEEE. Reprinted with permission.

Paper IV

M. Jansson, L. Harnefors, O. Wallmark, and M. Leksell, "Synchronization at startup and stable rotation reversal of sensorless nonsalient PMSM drives," *IEEE Transactions on Industrial Electronics*, vol. 53, no. 2, pp. 379-387, Apr. 2006.

IV

© 2006 IEEE. Reprinted with permission.

Paper V

O. Wallmark, O. Carlson, and L. Harnefors, "Loss minimization of a PMSM drive for a hybrid electric vehicle," in *Proc. 11th International Conference on Power Electronics and Motion Control (EPE PEMC'04)*, vol. 6, 2004, pp. 160–164.

V

Reprinted with kind permission of the EPE Association.

Paper VI

O. Wallmark, L. Harnefors, and O. Carlson, "Control algorithms for a fault-tolerant PMSM drive," in *Proc. 31st Annual Conference of the IEEE Industrial Electronics Society (IEEE IECON'05)*, 2005, pp. 1467-1473. The slightly revised version presented here is accepted for publication in *IEEE Transactions on Industrial Electronics*.

A black rectangular box containing the white Roman numeral 'VI' in a serif font.

© 2005 IEEE. Reprinted with permission.

Paper VII

M. Jonasson and O. Wallmark, “Stability of an electric vehicle with permanent-magnet in-wheel motors during electrical faults,” to be presented at the *22nd International Battery, Hybrid and Fuel Cell Electric Vehicle Symposium & Exposition (EVS’22)*.

A black rectangular box containing the Roman numeral VII in white serif font.

Reprinted with permission from the EVS-22 Program Committee.

Paper VIII

M. Jonasson and O. Wallmark, “Control of electric vehicles with autonomous corner modules: implementation aspects and fault handling,” submitted to the *International Journal of Vehicle Systems Modelling and Testing*.



